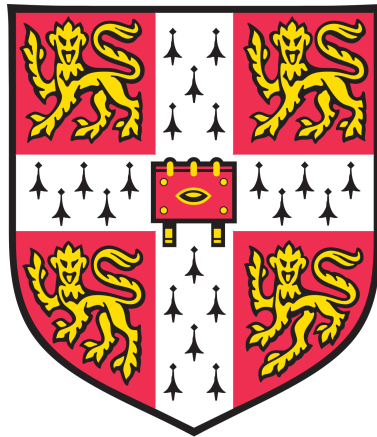


UNIVERSITY OF CAMBRIDGE
DEPARTMENT OF ENGINEERING

MASTERS PROJECT REPORT



Propulsion Systems for VTOL Electric Vehicles

Jordan Sandberg Eriksen

SUPERVISED BY: Dr Sam Grimshaw

Abstract

Abstract here..

Contents

1	Introduction	1
1.1	Literature Review	2
1.2	Measuring Propulsor Performance	2
1.3	Research Question	6
2	Flying Test Bed System Design	7
2.1	Flying Test Bed	7
3	Ducted Fan Aerodynamic Design	10
3.1	Introduction	10
3.2	Mean-line Design	10
3.3	3D Blade Design	17
4	Electrical and Mechanical Design	24
4.1	Introduction	24
4.2	Electrical Design	24
4.3	Mechanical Design	26
5	Experimental Methods	30
5.1	Cage Design & Tether	30
5.2	Stationary Propulsor Test	30
5.3	Hover Test	33
5.4	Measurement Techniques	34
6	Results	36
6.1	Stationary Propulsor Test	36
6.2	Hover Tests	44
7	Future Work	44
7.1	Propulsor Design	45
7.2	Stationary Propulsor Experiments	46
7.3	Flying Test Bed Experiments	46
8	Conclusions	48

Nomenclature

V_x	Axial flow velocity
Ω	
ϕ	Flow coefficient
ψ	Stage loading
Ω	rotor angular velocity
U	blade speed
r	radius
α	absolute flow angle relative to axial
β	rotor/upstream blade relative flow angle
γ	downstream blade relative flow angle
$-_\theta$	tangential
$-_x$	axial
$-_h$	hub
$-_c$	casing
$-_m$	mean-line



(a) Open propeller VTOL designs. **Left to right** Ehang 216 Autonomous Air Vehicle; Rolls-Royce VTOL; Wisk Cora eVTOL



(b) Ducted propeller/fan VTOL designs. **Left to right** Airbus Citybus; Bell NEXUS; Lilium Jet

Figure 1.1: Various propulsion systems used in recent eVTOL developments

1 Introduction

New aerospace markets are forecast to have a value of \$210-\$360 billion by 2040^[1], with the electric vertical take-off and landing (e-VTOL) sector trebling between 2019 - 2024^[2]. VTOL personal and unmanned goods transport reduces travelling time and does not require significant transport infrastructure to operate. Electric propulsion systems have zero emissions, lower running costs, and reduced noise output. Electric propulsion has opened up the design space with over 200 electrically propelled vehicles in development^[3] with different design solutions being explored as in Fig. 1.1. The key technical question is whether open or ducted propulsors are better. Ducted propulsors benefit from increased thrust for the same input power by increasing the pressure downstream of the propulsor and creating a low pressure region above it, however, ducting also adds weight. Ducted propulsors also benefit from improved safety as well as containment in an emergency situation. If the ducted fan power requirement for a specific application can match – or better – that of an open propeller, these additional benefits make the ducted fan the preferred propulsion method. Therefore the required application affects the choice of propulsor.

This report consolidates the design variables and presents a simple condition by which the performance of two candidate propulsors for an application can be compared. This condition is applied to the design of a ducted fan that aims to perform better than a VTOL optimised propeller when carrying a 1kg load. The condition is also used to explore the design space and suggest which applications could benefit from the use of ducted fans.

1.1 Literature Review

Studies on ducted fans have been conducted since the 1930s and a recent rise in research in the field, due to the interest in personal aerial vehicles (PAVs) as well as unmanned aerial vehicles (UAVs), has been noted. Zhang *et al.* (2020)^[4] presents the state of the art in ducted fan research and provides a full survey of around 90 published works. Research methods are divided into experimental, numerical modelling, computational fluid dynamics (CFD) and optimisation. Zhang shows experiments to test primarily ducted propellers (without stators) modelled using blade element theory and lifting line theory, as opposed to the turbomachinery approach based on turning and loss that is prevalent in turbo-jet and turbo-fan design. Extensive work has been undertaken on inlet geometry design for both static hover and cross-wind conditions. Exit duct area ratio is recognised as the primary factor affecting performance across all research methods, however Zhang comments on the lack of an integrated approach to design and optimisation. The six design challenges proposed by Zhang are: crosswind effects, tip clearance, high-speed performance, noise emissions, control systems, and contra-rotating ducted fan systems. The turbomachinery approach is an alternative method of analysis and design of ducted fans. Its performance against conventional propeller theory is unclear. Taking an integrated approach to propulsion system design for a specific application is also key to understanding how to improve on the performance of an open, though no work has been done on relating design point to the specific application. Contra-rotating systems are identified to be important for redundancy and torque balancing as well as having the potential to increase thrust density.

1.2 Measuring Propulsor Performance

1.2.1 Figure of Merit

The performance of a propulsor in hover can be quantified by the figure of merit, M_F , defined as a non-dimensional thrust-to-power ratio. From Pereira (2008)^[5]

$$M_F = \frac{T}{P} \sqrt{\frac{T}{2\rho A_x}} \quad (1.1)$$

where A_x , the blade passage axial flow area, can be related to the exit duct exit area, A_e , by the area ratio

$$\sigma = \frac{A_e}{A_x} \quad (1.2)$$

Considering the control volume around the ducted fan in Fig. ??, the thrust generated by the fan can be determined from the steady flow momentum equation (SFME). Assuming zero inlet swirl and straight and parallel exit flow (zero exit swirl), the static pressure at the duct exit, p_e , is equal to atmospheric pressure, p_a . Continuity gives the relationship between duct exit velocity and area ratio

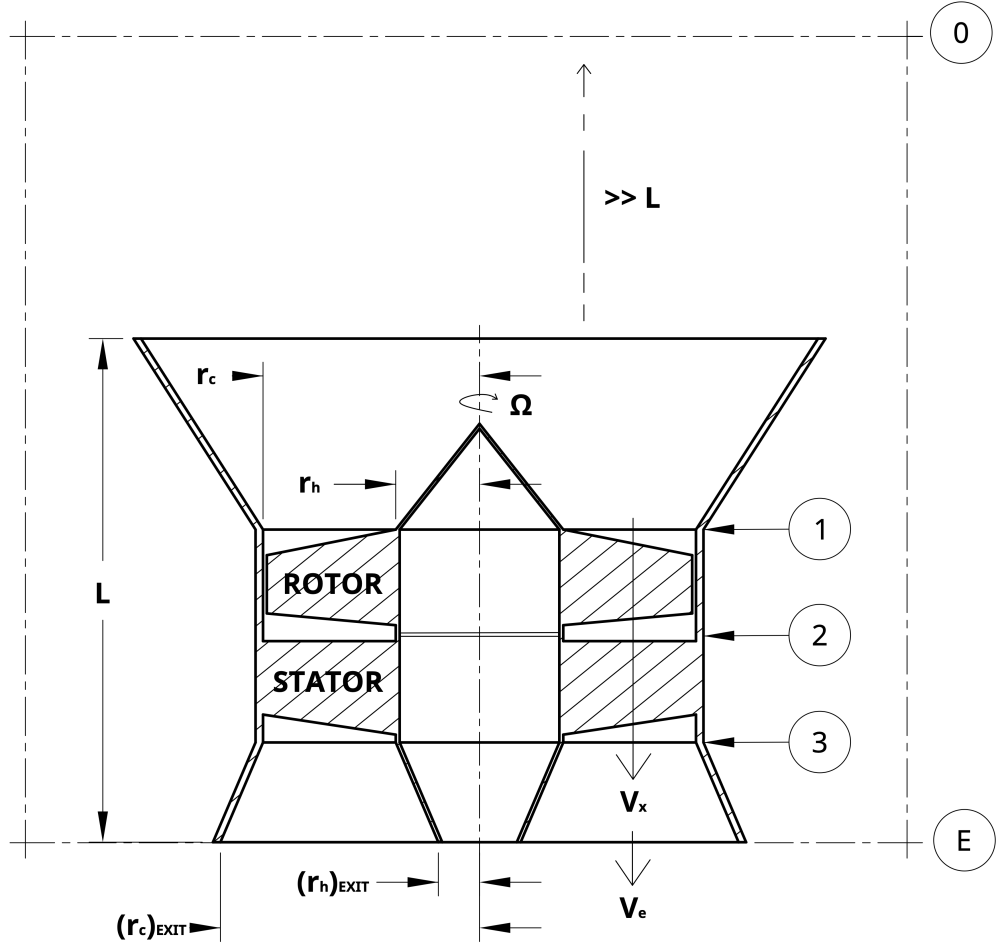


Figure 1.2: Ducted fan configuration and control volume. **0** Control volume inlet plane; **1** Rotor inlet plane; **2** Inter-rotor-stator plane; **3** Stator exit plane; **E** Exit duct/control volume exit plane.

$$\dot{m} = \rho A_x V_x = \rho A_e V_e \quad \therefore \sigma = \frac{V_x}{V_e} \quad (1.3)$$

Therefore the SFME can be written in terms of the blade passage quantities (A_x and V_x) and the area ratio, σ

$$T = \dot{m} V_e \quad \therefore T = \frac{\rho A_x V_x^2}{\sigma} \quad (1.4)$$

Flow power is determined from the steady flow energy equation (SFEE)

$$P = \frac{1}{2} \dot{m} V_e^2 \quad \therefore P = \frac{\rho A_x V_x^3}{2\sigma^2} \quad (1.5)$$

Substituting Eqn. 1.4 and Eqn. 1.5 into Eqn. 1.1 gives a simplified expression for figure of merit of a ducted fan:

$$M_F = \sqrt{2\sigma} \quad (1.6)$$

Therefore ducting the fan with an area ratio of $\sigma = 1$ gives a figure of merit of $M_F = \sqrt{2}$. Pereira (2008)^[5] shows the maximum figure of merit for a propeller to be 1. Provided the area ratio of the exit duct on a ducted fan remains $\sigma > 0.5$ the ducted fan figure of merit is greater.

1.2.2 Comparison of Ducted Fan and Propeller Performance

Although figure of merit characterises propulsor performance in static hover it does not consider the extra propulsor weight associated with a ducted fan (due to casing, intake, and diffuser) and the associated increase in required thrust. The power required for a propeller to maintain static hover – where the propulsor thrust is equal to the vehicle weight/ N_P (where N_P is the number of propulsors) – is calculated from the shaft figure of merit (calculated using shaft power) and the vehicle weight, W .

$$P = \frac{W/N_P}{(M_{F,s})_{prop.}} \sqrt{\frac{W/N_P}{2\rho A_{x,prop.}}} \quad (1.7)$$

Using the same power, the thrust obtainable with a ducted fan can be found by rearranging Eqn. 1.1

$$T_{fan} = \left[(M_{F,s})_{fan} P \sqrt{2\rho A_{x,fan}} \right]^{\frac{2}{3}} \quad (1.8)$$

For a given application, in order to perform better than a propeller, the thrust developed with the same power input must be greater than the new total vehicle weight. Expressing total thrust requirement in terms of the original vehicle weight and the extra weight due to the ducted fans gives

$$W \left(1 + \frac{\Delta W}{W} \right) < N_P \cdot T_{fan} \quad (1.9)$$

where ΔW is the extra weight of the vehicle due to the ducted fans. Combining Eqn. 1.8 and Eqn. 1.9 gives

$$W \left(1 + \frac{\Delta W}{W} \right) < N_P \left[(M_{F,s})_{fan} P \sqrt{2\rho A_{x,fan}} \right]^{\frac{2}{3}} \quad (1.10)$$

Using the thrust = weight condition satisfied by the propeller in Eqn 1.7, this can be rewritten as

$$W \left(1 + \frac{\Delta W}{W}\right) < \left[\frac{(M_{F,s})_{fan} \sqrt{A_{x,fan}}}{(M_{F,s})_{prop.} \sqrt{A_{x,prop.}}} \right]^{\frac{2}{3}} \cdot N_P \left[(M_{F,s})_{prop.} P \sqrt{2\rho A_{x,prop.}} \right]^{\frac{2}{3}} \quad (1.11)$$

Hence the requirement for the ducted fan to perform better than the propeller is

$$1 + \frac{\Delta W}{W} < \left[\frac{(M_{F,s})_{fan} \sqrt{A_{x,fan}}}{(M_{F,s})_{prop.} \sqrt{A_{x,prop.}}} \right]^{\frac{2}{3}} \quad (1.12)$$

Taking the theoretical figure of merit for the fan ($M_{F,s} = \sqrt{2\sigma}$) and propeller ($M_{F,s} = 1$) this becomes simply

$$\frac{W + \Delta W}{W} < \left[2\sigma \frac{A_{x,fan}}{A_{x,prop.}} \right]^{\frac{1}{3}} \quad (1.13)$$

where $W + \Delta W$ is the total weight of the flying test bed and ducted fans. Eqn. 1.13 provides two explicit design objectives:

1. Exit duct exit area should be maximised ($A_e = \sigma A_x$);
2. Ducted fan weight should be minimised

A trade-off arises as an increase in exit flow area will increase propulsor size and weight. Furthermore increasing exit duct area ratio above 1 means the exit duct becomes a diffuser. To prevent the flow in a diffuser from separating the length of diffuser required scales with the exit duct area ratio. In order to determine how this inequality can be satisfied the relationship between the geometric quantities on the RHS (σ and A_x) and the resulting propulsor weight must be found. This is achieved by creating a mass model that estimates the weight of the propulsor of given size and operating point, A_x and σ respectively. The difference between the RHS and LHS is Σ which gives the change in fan weight required as a percentage of payload and is used to quantify the inequality in Eqn. 1.13:

$$\Sigma = \left[2\sigma \frac{A_{x,fan}}{A_{x,prop.}} \right]^{\frac{1}{3}} - \frac{W + \Delta W}{W} \quad (1.14)$$

This is referred to as the “superiority parameter” as any design that satisfies this condition – that is gives a value of $\Sigma > 0$ – will require less power to maintain hover than an ideal propeller of a specified size and hence have superior performance.

1.2.3 Design Context

The ducted fans considered here are restricted by available manufacturing techniques. This introduces physical limits on the maximum size of propulsor that can be manufactured and tested. Ducted fans are to be 3D printed and so the size of the build plate limits the maximum

outer diameter of the propulsor to 185mm. The length of any cylindrical components is also limited by the vertical travel of the build plate to 200mm. The propulsor must therefore be designed within these limits. Given a fixed payload (defined by the weight of the flying test bed chassis) Eqn. 1.13 could be satisfied provided a large enough fan can be produced. This requirement is explored in the design section as the limiting size for the superiority condition to be satisfied can only be determined once a suitable mass model is developed.

1.3 Research Question

The research question proposed for this project is:

Are ducted fans more efficient than propellers in hover?

The size of the design space highlights the importance of a systems approach to the problem and therefore its multi-disciplinary nature. The question is broken down into 3 sub-questions.

1. Can a figure of merit of $M_{F,s} > \sqrt{2}$ be achieved using an exit duct area ratio of $\sigma > 1$?
2. For a specific application and design context can the superiority condition be satisfied?
3. Does performance in-flight reflect predicted performance from stationary tests?

These questions require a suitable platform to be developed to enable comparison of in-flight and stationary performance, as well as provide the design context and specific application required for the ducted fan design process.

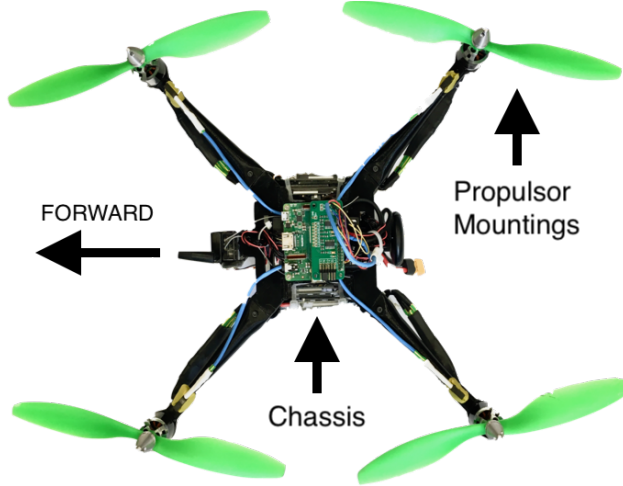


Figure 1.3: Image of flying test bed with propellers attached

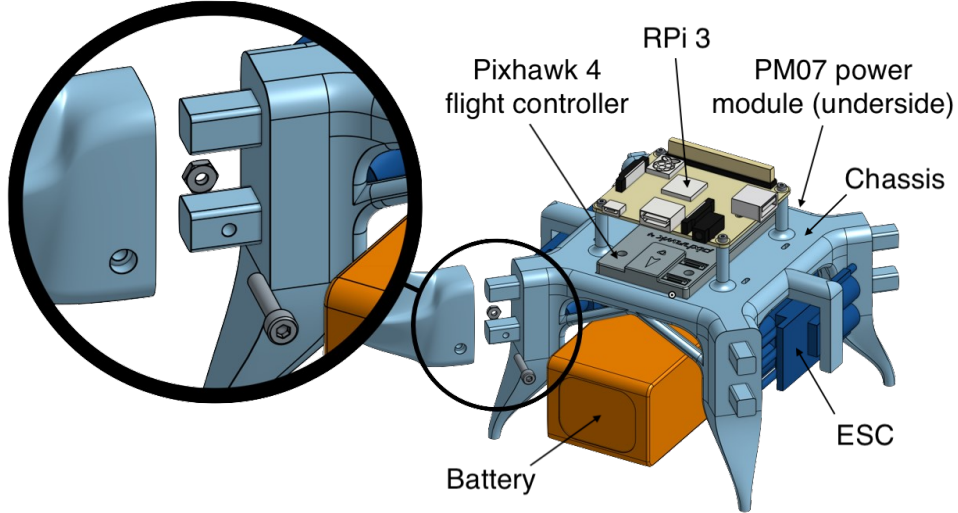


Figure 2.1: Flying test bed chassis showing exploded detail of double mortise and tenon joint for propulsor arms

2 Flying Test Bed System Design

The flying test bed is a system developed to enable testing of propulsors in a realistic environment. Its roles are to manage data collection and power supply during stationary tests, and control vehicle dynamics and collect data during hover tests.

2.1 Flying Test Bed

A UROP was conducted in the summer preceding this project during which an axi-symmetric quadcopter flying test bed was designed and manufactured. The two challenges addressed were structural design of the chassis, and the customisation of flight control hardware and software. The UROP concluded with successful flight of the flying test bed. During the 4th year project the flying test bed has been updated to allow measurements to be taken using both propellers and ducted fans in a stationary test and hover test configuration. “Off-the-shelf” 10in. propellers were used in the initial post-UROP flights (see Fig. 1.3).

2.1.1 Mechanical design

The test bed is designed to be rapidly 3D printable, light weight – whilst maintaining structural integrity – and modular to allow various propulsors and instrumentation to be mounted. Instrumentation management and flight hardware are mounted on a central chassis that is 3D printed as one piece for rigidity and to reduce complexity. Cantilevered propulsor arms are attached to the central chassis with a double mortise and tenon style mount, fastened by one M3 cap-head as in Fig. 2.1. Modularity allows for design iteration and rapid part replacement if required.

The following hardware is mounted directly onto the central chassis:

- **Pixhawk 4 Flight Control hardware** – Packaged, customizable autopilot hardware
- **PM07 Power Module** – Power module managing distribution of power from battery/power supply to flight controllers, other on-board computers, and motors
- **Raspberry Pi 3 Model A+** – On-board computer managing data acquisition and assisting flight controller automation
- **ADCPi ADC Breakout** – Analogue to digital converter mounted directly to the Raspberry Pi 3
- **4x Aerostar 50A ESC** – Electronic Speed Controller driving BLDCM motors
- **Optional: Turnigy 5000mAh 14.8V (4-cell) Battery** – Large capacity 14.8V (nominal) battery. Can be replaced by a tethered 12V power supply.

The central chassis has dimensions of approximately 125mm x 139mm x 93mm. It has a dry mass (excluding battery) of 0.529kg and the battery has a mass of 0.466kg.

2.1.2 Customisation of *Pixhawk 4* flight hardware/software

Pixhawk 4 is a packaged flight control hardware system running open source PX4 firmware. Interaction with the system is via the GUI QGroundControl and either a wireless telemetry transmitter-receiver pair or a serial connection (such as a USB). QGroundControl allows a predetermined automated flight path to be followed or alternatively the hardware can be configured to allow manual control provided adequate control inputs can be provided (a 16-channel remote with an 8-channel PPM-PWM converter is used here). The PM4 firmware includes various airframe configuration profiles, enabling it to adapt to the vehicle configuration and motor layout. The flying test bed is configured as a symmetric ‘X’ quadcopter. The profile was tuned to the flying test bed by varying PID gains on the control software, ensuring stable operation in hover. It provides a stable hover mode that is intended to reduce horizontal position deviation and maintain a fixed altitude. This means only small corrective inputs are required from the operator to ensure near stationary hover even in enclosed environments. It was found however that wall effects can be significant and so care must be taken when operating in such environments.

2.1.3 Subsystem Functions

Raspberry Pi 3 Model A+ (RPi3)

The RPi3 is a light-weight, small-footprint, 64-bit quad-core processor with UNIX-based operating system and Wi-Fi connectivity that can be run ‘blind’ through an SSH connection from a remote machine. It provides data acquisition and on-board data processing in Python and is used to pre-process test data before wirelessly transferring it back to the

remote machine. RPi3 has 28 general purpose input/output (GPIO) pins as well as I²C and serial interfaces among others.

ADCPi ADC Breakout

The ADC breakout board is designed specifically for the RPi3. Operating through the I²C interface, each breakout board provides an 8-channel ADC at 11 to 17 bit resolution with sample rates of 240 Hz to 3.75 Hz sample rate respectively.

PM07 Power Module

Designed to operate in tandem with the Pixhawk 4 flight controller, the PM07 provides power control for the high-power outputs (such as the motors) as well as a regulated 5V output for the flight controller and RPi3. Power input is 7-51V DC and the output current is limited to 120A (approximately 30A per propulsor). The battery selected can operate up to 125A to accommodate this demand. PM07 also provides 2 ADC inputs.

2.1.4 Subsystem Interaction

Pixhawk 4 provides simple subsystem interaction through its input ports. 5 ports connect the flight controller to the power module: 2x power inputs, 1x motor PWM outputs, 1x auxiliary PWM output, and 1x ADC input. The serial port on the Pixhawk 4 is rewired to connect to the RPi3's UART TXD and RXD terminals. The I²C port connects to an I²C bus that allows up to 5 devices to interface with the Pixhawk 4, including 3 ultrasound sensors measuring proximity in the x, y, and z directions. These sensors can optionally be connected via the ADC for use by the RPi3. Figure 2.2 shows schematically how the subsystems interact.

2.1.5 Telemetry

Pixhawk 4 wireless telemetry

The “plug-and-play” telemetry module allows wireless connection to the Pixhawk 4 from a ground control station on a remote machine such as QGroundControl. This is used to communicate with the Pixhawk 4 about flight control and to log power usage data (PM07 voltage and current output).

SSH/SCP on RPi3

RPi3 is wireless enabled allowing it to be accessed remotely via the SSH (secure shell) protocol. SCP (secure copy protocol) allows files to be copied to and from the RPi3. This is used after data collection to collect all data on the remote machine. A dedicated wireless router is used to connect the RPi3 to a remote machine – done automatically on start-up of the RPi3.

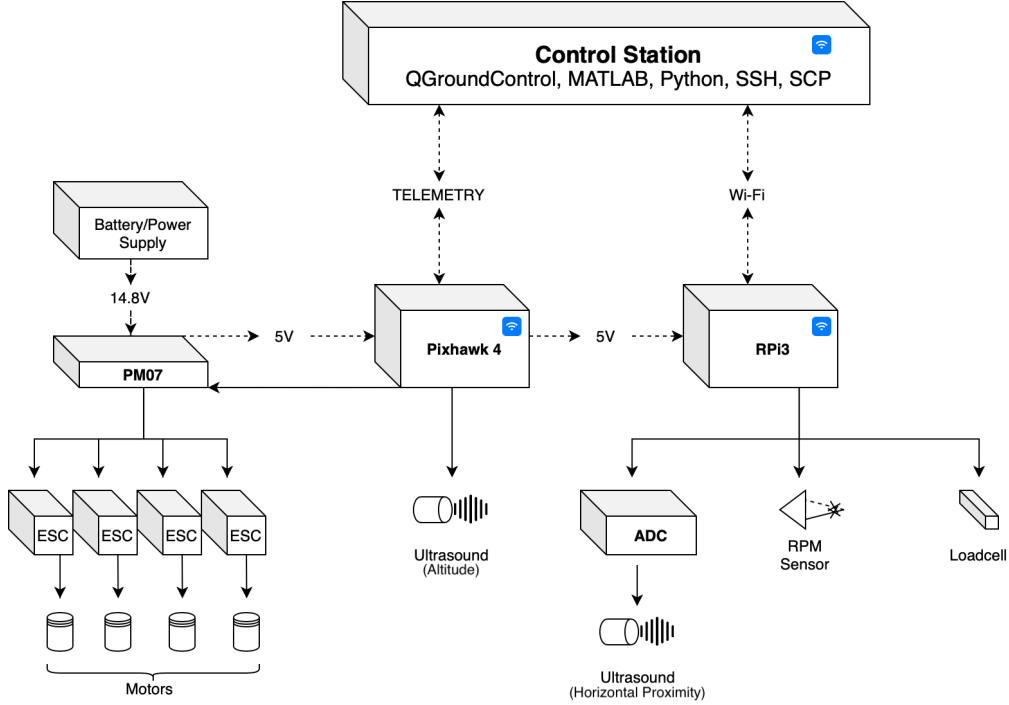


Figure 2.2: Subsystem schematic of flying test bed

3 Ducted Fan Aerodynamic Design

3.1 Introduction

This section describes the aerodynamic design of an electric ducted fan, 3D printed in PLA, that is designed to replace a propeller on a VTOL electric vehicle. The flying test bed is powered by 4 propulsors and is designed to achieve steady hover with a payload equal to the weight of the flying test bed. Figure 1.2 shows a schematic of the ducted fan configuration and the design process is summarised by the flow chart in Fig. 3.1.

3.2 Mean-line Design

The propulsor design at mean-line is described below. The choice of mean-line location for a low hub-to-tip ratio (HTR) machine is discussed and validated.

3.2.1 Non-dimensional Operating Point

Blades design is determined by the choice of non-dimensional operating point given by flow coefficient (Eqn. 3.1a) and stage loading (Eqn. 3.1b) where the mean-line blade velocity is $U = \Omega \cdot r_m$ with r_m equal to the mean-line radius.

$$\phi = \frac{V_x}{U} \quad (a) \qquad \psi = \frac{\Delta h_0}{U^2} \quad (b)$$

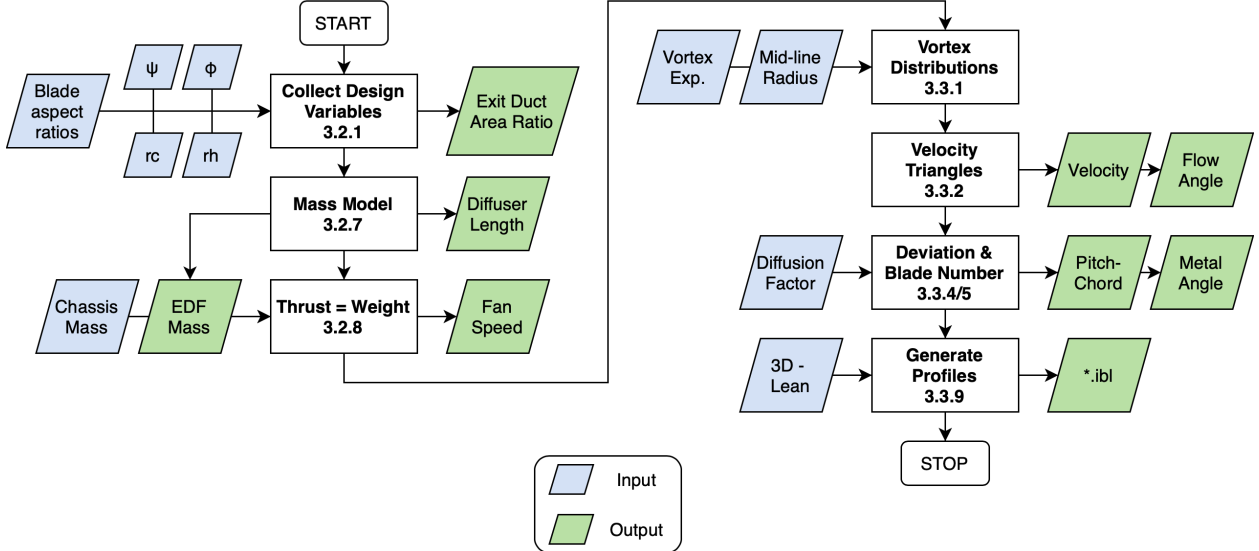


Figure 3.1: Flow chart showing the aerodynamic design process. 2D design stages are on the left and the 3D design stages are on the right. Processes are labelled by the report section in which they appear (3.x.x)

Assuming isentropic flow, stage loading can be written in terms of the stagnation pressure rise, Δp_0 . Using Bernoulli and the assumption exit static pressure is equal to atmospheric gives an expression for Δh_0 in terms of axial blade passage velocity V_x and area ratio.

$$\Delta p_0 = (p_0)_e - (p_0)_{in} = (p_e + \frac{p_a}{2}\rho V_e^2) - p_a$$

$$\Delta p_0 = \frac{1}{2}\rho V_e^2$$

$$\Delta h_0 = \frac{\Delta p_0}{\rho} \quad (3.2)$$

$$\Delta h_0 = \frac{V_x^2}{2\sigma^2} \quad \therefore \psi = \frac{V_x^2}{U^2} \cdot \frac{1}{2\sigma^2} \quad (3.3)$$

Therefore ϕ , ψ , and σ are related by

$$\psi = \frac{\phi^2}{2\sigma^2} \quad (3.4)$$

The operating point can therefore be defined by the area ratio, σ and the flow coefficient, ϕ . This allows the corresponding stage loading to be specified and resulting figure of merit determined.

3.2.2 Fan Operating Speed

Equation 1.6 shows that the figure of merit for a ducted fan in hover is independent of the speed of rotation of the fan. The fan speed, however, impacts the magnitude of thrust developed, shown by substituting Eqn. 3.1a into Eqn. 1.4.

$$T = \frac{\rho A_x (\Omega r_m \phi_m)^2}{\sigma} \quad (3.5)$$

This shows thrust to vary with both fan speed and fan size, and so required thrust varies depending on the choice of these parameters. The effect of fan size is discussed in section 3.2.6.

3.2.3 Mean-line Location

Maximising the flow area for a given propulsor radius maximises thrust developed (Eqn. 3.5) and ensures minimum use of material and therefore a lighter design. This results in a small hub radius (limited only by electric motor size, typically $\approx 20mm$) and consequently low hub-to-tip ratios (< 0.5). Selecting a mean-line at the mid-span radius gives different mass flows above and below the mean-line and this results in variation in loading across the span. An alternative mean-line position is defined by balancing the mass flow above and below the mean-line. This sets the mean-line radius at the root-mean-square of the hub and tip radii

$$r_m = \sqrt{\frac{r_h^2 + r_c^2}{2}} \quad (3.6)$$

3.2.4 Overall Performance

Expressions for fan thrust and power can now be determined in terms of the non-dimensional operating point and the fan's geometric variables as in Eqn. 3.7 and Eqn. 3.8.

$$T = \frac{\rho \pi \phi_m^2 \Omega^2 (r_c^4 - r_h^4)}{2\sigma} \quad (3.7)$$

$$P = \frac{\rho \pi \phi_m^3 \Omega^3 (r_c^2 - r_h^2)}{2\sigma^2} \left(\frac{r_c^2 + r_h^2}{2} \right)^{\frac{3}{2}} \quad (3.8)$$

3.2.5 Mass Model

In order to solve the superiority condition a mass model is required to relate estimated propulsor weight to design variables σ , r_c , and r_h . Figure 3.2 shows an exploded view of the components making up the mass model. The diffuser hub and casing, and the intake are modelled as hollow truncated cones. The blade duct hub and casing are modelled as hollow cylinders. Blade rows are modelled as thin annular disks.

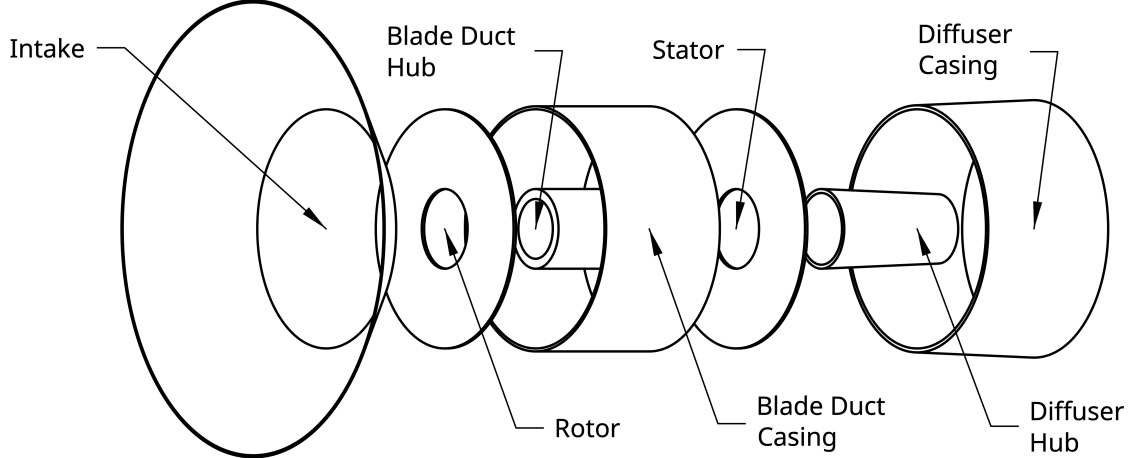


Figure 3.2: Exploded view of ducted fan mass model components

Diffuser ESDU 75026^[6] presents the performance of symmetric annular diffusers in incompressible flow. The length of diffuser required to prevent separation is estimated from Fig. 3 in ESDU 75026 which gives empirical limits of separation at various length and area ratios for symmetric annular diffusers. Considering Eqn. 1.3 and Bernoulli's equation, static pressure recovery can be written as

$$C_{pr} = \frac{p_e - p_x}{\frac{1}{2}\rho V_x^2} = 1 - \frac{1}{\sigma^2} \quad (3.9)$$

where p_x is the static pressure at entry to the exit duct. Figure ?? shows two limit lines, C_{pr}^* and C_{pr}^{**} representing the separation limit and the limit of performance due to frictional loss and boundary layer growth respectively. Designing on the appropriate constant C_{pr} line close to C_{pr}^{**} will produce a diffuser that is unlikely to separate. This line can be approximated with an R-squared value of 0.9999 by

$$\frac{L_{diff.}}{r_c - r_h} = -5.56\sigma^3 + 24.16\sigma^2 - 23.41\sigma + 5.413 \quad (3.10)$$

The diffuser hub and casing are modelled as hollow truncated cones with height $L_{diff.}$ (determined by Eqn. 3.10), a base radius r_h (for the hub) and $(r_c)_{exit}$ (for the casing), a truncation radius of $(r_h)_{exit}$ (for the hub) and r_c for the casing, and a thickness t , as in Fig. 1.2. Diffuser exit hub and casing radius for a symmetric diffuser can be found by considering the equal flow angle at the hub and casing giving

$$\frac{(r_c)_{exit} - r_c}{L} = \frac{r_h - (r_h)_{exit}}{L} \quad (3.11)$$

$$\therefore (r_c)_{exit}, (r_h)_{exit} = \frac{r_c + r_h}{2} \pm \frac{\sigma}{2}(r_c - r_h) \quad (3.12)$$

Equation 3.13 gives the volume of a hollow truncated cone using the variables defined in Table 3.1 allowing the total mass of the diffuser to be determined.

	Hub value	Casing value
R	r_h	$(r_c)_{exit} + t$
r	$(r_h)_{exit}$	$r_c + t$
S	$r_h - t$	$(r_c)_{exit}$
s	$(r_h)_{exit} - t$	r_c
h	$L_{diff.}$	$L_{diff.}$

Table 3.1: Parameter values for diffuser hub and casing

$$V = \frac{h\pi}{3}(R^2 + Rr + r^2 - S^2 - Ss - s^2) \quad (3.13)$$

$$m_{diff.} = \rho_{PLA}(V_{hub} + V_{case}) \quad (3.14)$$

Blade Passage The blade passage (excluding rotor and stator blades) is modelled as a straight annulus 3D printed in PLA. The passage itself has inner radius r_h and outer radius r_c . The casing is modelled to have thickness of $t_c = 1.5mm$ and the hub section has a thickness of $t_h = 5mm$. The length of the blade passage is $L_{BP} = 70mm$ giving a total mass of

$$m_{BP} = \rho_{PLA}L_{BP}\pi[2r_h t_h - t_h^2 + 2r_c t_c + t_c^2] = 2.73r_h + 0.818r_c - 0.0062 \quad (3.15)$$

Intake For simplicity the intake is also modelled as a hollow truncated cone, an approximation for its actual ellipsoidal geometry. It has approximately equal length to its change in radius which is set equal to $1.5 \times r_c$. Therefore using Eqn. 3.13, and assuming a thickness of $1mm$, the intake mass can be approximated by

$$m_{in.} = 3.90(r_c - r_h)(3r_c - r_h + 0.001) \quad (3.16)$$

Blades As the number of blades has not yet been determined, the blades are modelled as having the equivalent mass of an annular flat disk of thickness $t_{rotor} = 1.5mm$ for the rotor and $t_{stator} = 1.5mm$ for the stator. The resulting mass is given by

$$m_{blades} = \rho_{PLA}\pi(r_c^2 - r_h^2)(t_{rotor} + t_{stator}) \quad (3.17)$$

$$m_{blades} = 11.7(r_c^2 - r_h^2) \quad (3.18)$$

Thrust–Weight Balance The mass model described above provides an approximation for the mass of a particular design. In hover, the load carried by each propulsor is equal to the propulsor weight and its share of the payload weight (4 propulsors). The payload here is the flying test bed chassis and battery, described in section 2.1. Using Eqn. 3.7 the thrust developed can be set equal to the required thrust to give the relationship between the design variables when the propulsor is operating in the static hover state.

$$T = g \left[m_{fan} + \frac{m_{chassis}}{4} + \frac{m_{battery}}{4} \right] \quad (3.19)$$

$$\frac{\rho\pi\phi_m^2\Omega^2(r_c^4 - r_h^4)}{2\sigma} = g[m_{diff.} + m_{BP} + m_{in.} + m_{blades} + m_{motor}] + 2.44N \quad (3.20)$$

3.2.6 Design Selection

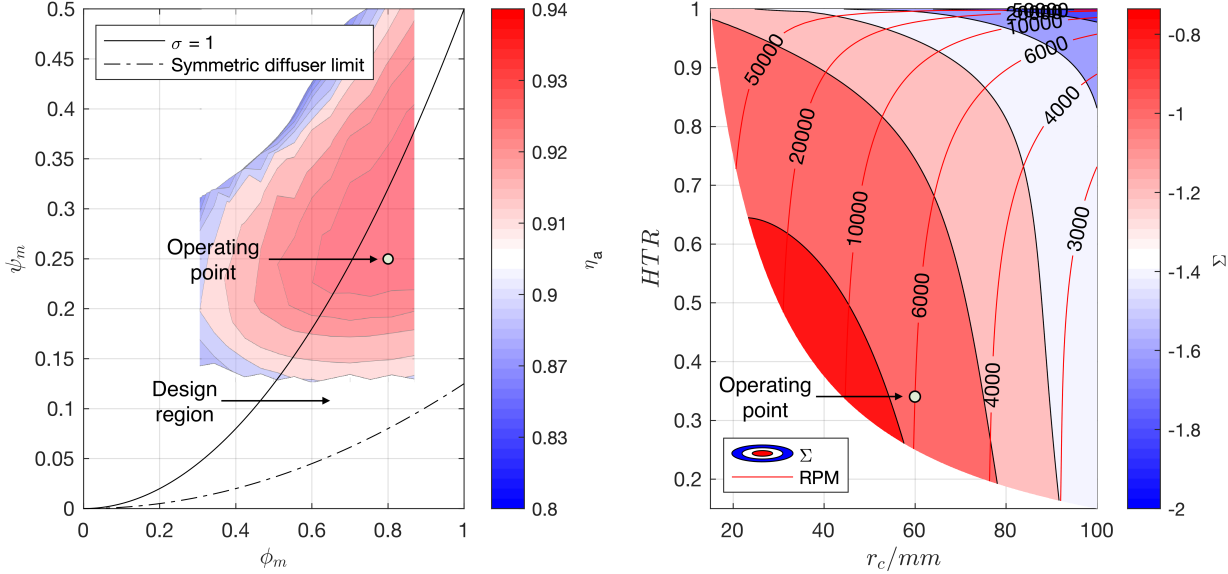
The following constraints and objectives are imposed on the design space. They are considered in the following order:

1. Design in a high efficiency region for low Reynolds number blades
 - Choose operating point for ϕ and ψ , hence determine σ
2. Satisfy the superiority condition (Eqn. 1.13)
 - Minimise propulsor mass
 - Maximise flow area and exit duct area ratio
 - Choose geometric design point for r_c and HTR
3. Operate in a suitable speed-torque regime for the electric motor
 - Calculate operating point for Ω based on T , σ , and ϕ as in Eqn. 3.5

The resulting design point is shown in Table 3.4.

Blade Operating Point Figure 3.3a shows a Smith Chart for the Maffioli *et al.* (2015)^[7] low Reynolds number blade profiles used in this design, overlaid on the ϕ_m - ψ_m design space. The design region has a limit of $\sigma = 1$ to obtain a design figure of merit of $M_F > \sqrt{2}$, as well as a symmetric diffuser limit arising from the diffuser hub converging to a point. The contours show that blade efficiency in a 2D cascade decreases for flow coefficients $\phi_m < 0.6$ and stage loading $\psi_m < 0.2$. This is verified by Corralejo *et al.* (2017)^[8]. The operating point of $\phi_m = 0.8$, $\psi_m = 0.25$ is chosen as it lies in the middle of this design region. This gives an exit duct area ratio of $\sigma = 1.1314$.

Geometric Design Point Using the mass model the superiority condition is determined in terms of the free variables r_c and HTR for $\sigma = 1.1314$, a fixed propeller area $A_{x,prop.}$, and assumed ideal propeller figure of merit as in Eqn. 3.21. As discussed in Section 1.2.3 the maximum size of the propulsor is limited by manufacturing methods. The minimum hub radius is determined by the size of the electric motor (typically $r_h > 15\text{mm}$) and so the design space explored is defined by $15\text{mm} \leq r_c \leq 100\text{mm}$ and a HTR range of $0 \rightarrow 1$ (provided $r_h > 15\text{mm}$). Figure 3.3b shows the value of the difference between the RHS and LHS of the superiority condition, Σ , which must be positive for the condition to be satisfied.



(a) Blade operating point design space shown with exit duct area ratio limits and Maffioli (2015) Smith chart overlaid. Note non-linear color bar

(b) Superiority condition across the r_c -HTR geometric design space. Contours of required RPM are overlaid

Figure 3.3: Blade aerodynamic and propulsor geometric design spaces

$$\Sigma = \left[\frac{2\sigma}{1} \frac{A_{x,fan}}{A_{x,prop}} \right]^{\frac{1}{3}} - \left(\frac{W + \Delta W}{W} \right) \quad (3.21)$$

Figure 3.3b shows Σ to be negative throughout this design region of interest (defined by 1kg payload, fixed σ and manufacturing method) meaning the superiority condition is not satisfied. Though not achievable in this region, being able to achieve a high figure of merit maximises the design region that satisfies the superiority condition elsewhere in the design space (for example increased payload and lighter materials). At larger payloads and through the use of advanced materials, the ratio of $\Delta W/W$ decreases allowing the condition to be satisfied. This is explored in Section ???. Therefore a design that does not satisfy the superiority condition but achieves $M_F > \sqrt{2}$ is chosen. Increasing HTR reduces the flow area hence reducing $A_{x,fan}/A_{x,prop}$. The reduction in ΔW resulting from a decrease in inlet and diffuser mass is outweighed by the reduction in $A_{x,fan}/A_{x,prop}$, and so lower values of Σ are observed at high HTR. The nearest design region to satisfying the condition is at low values of r_c and low values of HTR. As r_c decreases, the motor speed required to maintain hover thrust increases significantly (see Eqn. 3.7) and so a casing radius of 60mm and a HTR of $1/3$ is chosen, giving a hub radius of 20mm and a predicted $\Sigma = -0.84$.

Electric Motor Operating Point The mass model is used to estimate the weight of the

ϕ_m	0.80
ψ_m	0.25
σ	1.1314
$L_{diff.}$	72.0 mm
r_c	60 mm
r_h	20 mm
r_m	44.7 mm (RMS)
Ω	6000 RPM

Figure 3.4: Propulsor design point

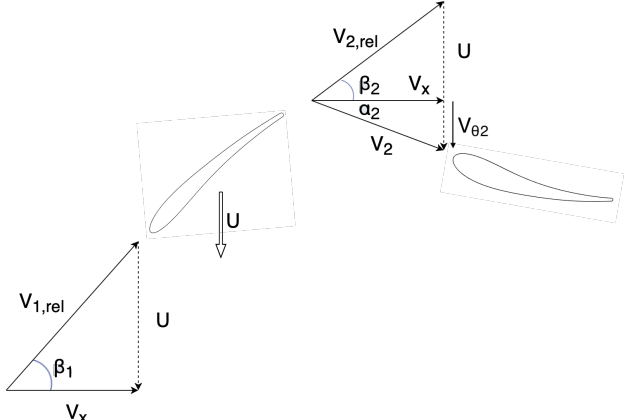


Figure 3.5: Mean-line velocity triangles (stator exit omitted as flow axial at exit)

ducted fan propelled vehicle and therefore determine the thrust required ($T = W/N_P$). Equation 3.7 is used to calculate the rotor speed required to achieve this thrust:

$$\Omega = \sqrt{\frac{2\sigma \frac{W}{N_P}}{\rho \pi \phi_m^2 (r_c^4 - r_h^4)}} \quad (3.22)$$

$$\therefore \Omega = 627.5 \text{ rad} \cdot \text{s}^{-1} = 5992 \text{ RPM} \approx 6000 \text{ RPM} \quad (3.23)$$

Velocity Triangles Now the design parameters have been determined the mean-line velocity triangles can be drawn for this particular design. Figure 3.5 shows the velocity triangles in context with rotor and stator blades. Flow angles are measured positive in the sense of rotor rotation (in Fig. 3.5 positive down).

3.3 3D Blade Design

Overall performance has been determined by setting the mean-line values of flow coefficient, ϕ_m , and stage loading, ψ_m . The values of ϕ and ψ must vary along the span as the local value of blade speed changes, and for equilibrium to be maintained across the flow passage. In order to satisfy these conditions the radial equilibrium equation must be satisfied.

3.3.1 3-dimensional Flow Solutions to Radial Equilibrium

Radial equilibrium states that for axi-symmetric and incompressible annulus flow Eqn. 3.24 must be satisfied.

$$\frac{dh_0}{dr} - T \frac{ds}{dr} = V_x \frac{dV_x}{dr} + \frac{V_\theta}{r} \frac{d(rV_\theta)}{dr} \quad (3.24)$$

Assuming there is no variation in stagnation enthalpy or entropy across the span, this reduces to

$$V_x \frac{dV_x}{dr} + \frac{V_\theta}{r} \frac{d(rV_\theta)}{dr} = 0 \quad (3.25)$$

Noting Eqn. 3.1 and applying Euler's work equation, we obtain

$$\phi r \frac{d(\phi r)}{dr} + \psi \frac{d(\psi r^2)}{dr} = 0 \quad (3.26)$$

Which has general solutions in the form

$$\phi = \phi_m \left(\frac{r}{r_m} \right)^A \quad (a) \qquad \psi = \psi_m \left(\frac{r}{r_m} \right)^B \quad (b) \quad (3.27)$$

where ϕ_m and ψ_m are the mean-line quantities. Substituting eqns. 3.27a & 3.27b into Eqn. 3.26 gives

$$\begin{aligned} \left[\phi_m \left(\frac{r}{r_m} \right)^A \right]^2 (1 + A) &= - \left[\psi_m \left(\frac{r}{r_m} \right)^B \right]^2 (2 + B) \\ \therefore \phi^2 (1 + A) &= -\psi^2 (2 + B) \end{aligned} \quad (3.28)$$

This solution can be used to determine the values of the exponents, A and B . The constant B is referred to here as the vortex distribution exponent as it determines the tangential velocity variation in the r - θ plane.

Free Vortex ($B = -2$) One such distribution arises from the free vortex condition. This results from the solution to Eqn. 3.28 in which both LHS and RHS are equal to zero giving

$$A = -1 \quad (a) \qquad B = -2 \quad (b) \quad (3.29)$$

Therefore from Eqn. 3.27a and Eqn. 3.29a

$$\phi(r) \sim \frac{1}{r} \qquad \therefore \frac{d}{dr}(V_x) = 0 \quad (3.30)$$

Axial velocity across the span is constant and it can be shown from Eqn. 3.27b and Eqn. 3.29b

$$\psi(r) \sim \frac{1}{r^2} \qquad \therefore \frac{d}{dr}(\Delta h_0) = 0 \quad (3.31)$$

Therefore the loading is equal across the span and $V_{\theta 2} \sim 1/r$ resulting in a vorticity free (lowest loss) flow^[9]. Both the constant V_x and the constant Δh_0 conditions indicate uniform exit static pressure. In practice the variation in $V_{\theta 2}$ across the span results in large variations in blade twist angle that should be avoided (see Fig. 3.6 that shows $V_{\theta 2}$ variation resulting in over 20° of absolute flow angle variation). Furthermore, Fig. 3.6 shows stage loading, ψ , to become larger than 1 at radii close to the hub. From Euler, and given axial inlet flow

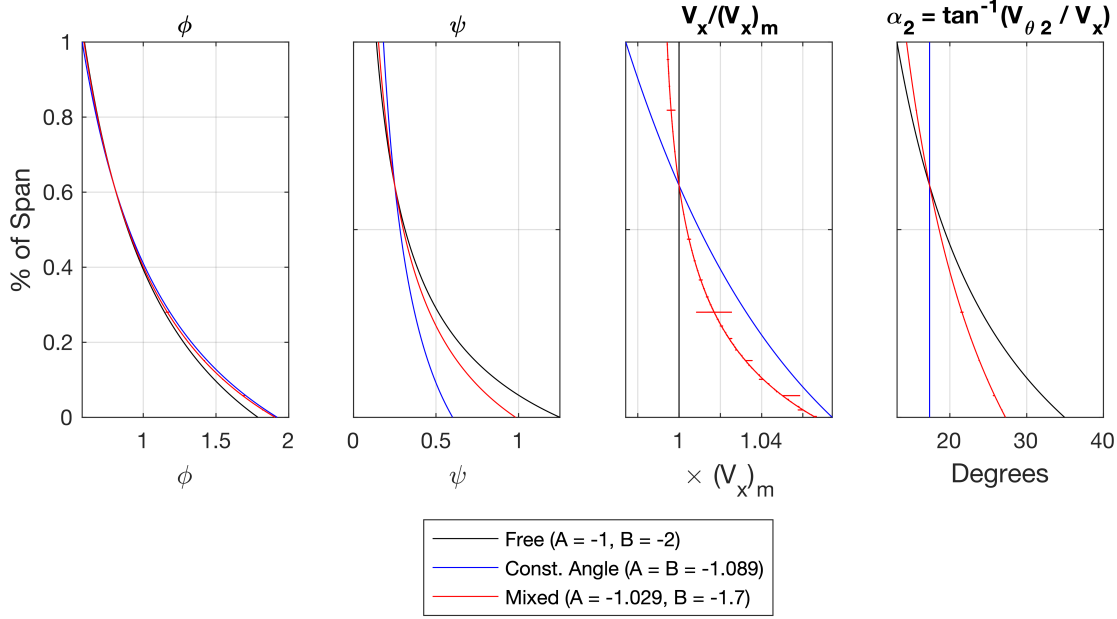


Figure 3.6: Distributions of design parameters ϕ and ψ and non-dimensionalised axial and tangential velocities, V_x and $V_{\theta 2}$ respectively, across the span at 3 different boundary conditions (free vortex, constant angle and mixed vortex).

$$\Delta V_\theta = V_{\theta 2} = \psi U \quad (3.32)$$

This shows the tangential velocity at the hub to be greater than the local blade speed. By reducing the value of the vortex distribution exponent, B , this can be avoided as $\psi_{hub} \leq 1$.

Mixed Vortex ($-2 \leq B \leq 0$) Equation 3.28 can also be used to numerically solve the radial equilibrium equation for any value of the vortex distribution exponent provided ϕ_m and ψ_m are known. The mixed vortex design shown in Fig. 3.6 has a vortex distribution exponent of -1.7 . This produces a vortex distribution that, at the hub, has a tangential velocity equal to the velocity of the hub wall. This reduces the absolute velocity of the flow past the wall and therefore reduces frictional loss at the hub. Hereafter any reference to a ‘mixed vortex condition’ corresponds to a vortex distribution exponent of $B = -1.7$, as described here.

Constant Angle Another common design is for constant absolute flow angle across the span, such that

$$\frac{d}{dr} \left(\frac{V_\theta}{V_x} \right) = 0 \quad (3.33)$$

$$\therefore \frac{\psi}{\phi} = constant \left(= \frac{\psi_m}{\phi_m} \right) \quad (3.34)$$

This results in the exponents A and B being equal giving

$$A = B = -\left(\frac{2\psi_m^2 + \phi_m^2}{\psi_m^2 + \phi_m^2}\right) \quad (3.35)$$

3.3.2 3D Velocity Triangles

Once the distributions of ϕ and ψ have been determined the variation in flow velocities and angles can be found across the span. The value of any velocity or angle can be found using the appropriate local values of the spanwise variables ϕ , ψ , U , and r . The relative merits of each of the vortex distributions are discussed in Section 6 in which the three designs presented here are tested.

3.3.3 Validation of Mean-line Location

Eqn. 3.7 and Eqn. 3.8 come from the assumption that mean-line design parameters are representative of the performance of the whole flow. This assumption can be verified now that the span-wise distribution of the flow parameters has been determined. Integrating the work done and thrust generated by an infinitesimal annulus element allows the real power and thrust produced by the propulsor to be determined. This is computed numerically and the expression obtained above for each of the parameters in Eqn. 3.38.

$$P = \int_{r_h}^{r_c} \Delta h_0 \cdot d\dot{m} \quad (3.36)$$

$$\Delta h_0 = \psi U^2 \quad (a) \qquad d\dot{m} = \rho V_x (2\pi r dr) \quad (b) \quad (3.37)$$

$$\therefore P = 2\pi\rho\Omega^3 \cdot \frac{\phi_m\psi_m}{r_m^{B+A}} \int_{r_h}^{r_c} r^{A+B+3} dr \quad (3.38)$$

A similar expression can be obtained for the thrust developed. The mass-averaged mean-line radius definition of r_m is compared to the conventional mean-line radius definition of r_m in Table 3.2 by calculating the error between the integral power and thrust and that predicted from Eqn. 3.8 and Eqn. 3.7. A properly balanced mean-line radius choice ensures the integral power is as close to the predicted one as possible, minimising the error

Mean-line radius	P error	T error
$r_m = \text{mean}(r_c, r_h)$	37%	24%
$r_m = RMS(r_c, r_h)$	1.2%	0.36%

Table 3.2: Comparison of mean-line predicted and integral power and thrust from different mean-line definitions

Table 3.2 shows that selecting a mean-line radius at the RMS of the hub and casing radius reduces the error between the integral and the predicted power requirements to $\approx 1\%$. These errors are small enough to be neglected and so this choice of mean-line radius is validated.

3.3.4 Blade Number and Span-wise Chord

Lieblein *et al.* (1953)^[10] present a correlation for diffusion factor as a function of velocities and the pitch-chord ratio of the blades.

$$DF = \left(1 - \frac{V_{2,rel}}{V_{1,rel}}\right) + \left(\frac{V_{\theta 1,rel} - V_{\theta 2,rel}}{2V_{1,rel}}\right) \frac{s}{c} \quad (3.39)$$

This expression is valid for both the rotor and stator provided the relative values are taken in the respective blade's frame off reference. Having determined the span-wise variation in the flow velocities and angles, the value of the local pitch-chord ratio, s/c , can be found provided a suitable diffusion factor is chosen. Consider first a constant value of diffusion factor that lies below the separation limit suggested in CUED Turbomachinery I^[11] as $DF_{lim.} = 0.6$, such as $DF = 0.45$. Pitch-chord across the span can be determined as

$$\frac{s}{c} = \left[DF - \left(1 - \frac{V_{2,rel}}{V_{1,rel}}\right)\right] \left(\frac{2V_{1,rel}}{V_{\theta 1,rel} - V_{\theta 2,rel}}\right) \quad (3.40)$$

In order to determine span-wise pitch, the number of blades are determined using the mean-line values. The mean-line chord is estimated using the blade mean-line aspect ratio where $AR = span/chord = l/c$

Vortex Design	Diffusion Factor	Rotor		Stator	
		N_R	Selected	N_S	Selected
Free Vortex	$DF = 0.45$	(5.60)	7	(4.66)	5
	$0.25 \leq DF \leq 0.4$	(10.48)	11	(7.20)	7
Mixed Vortex	$DF = 0.45$	(5.60)	7	(4.66)	5
	$0.25 \leq DF \leq 0.4$	(10.48)	11	(7.20)	7
Constant Angle	$DF = 0.45$	(5.60)	7	(4.66)	5
	$0.25 \leq DF \leq 0.4$	(10.48)	11	(7.20)	7

Table 3.3: Rotor and stator blade numbers at various design conditions

$$c_m = \frac{r_c - r_h}{AR} \quad (3.41)$$

$$N = \frac{2\pi r_m}{(s/c)_m c_m} \quad (3.42)$$

The blade number is rounded up to the next integer value. Table 3.3 at the end of this section outlines the calculated and selected blade numbers for each of the designs discussed.

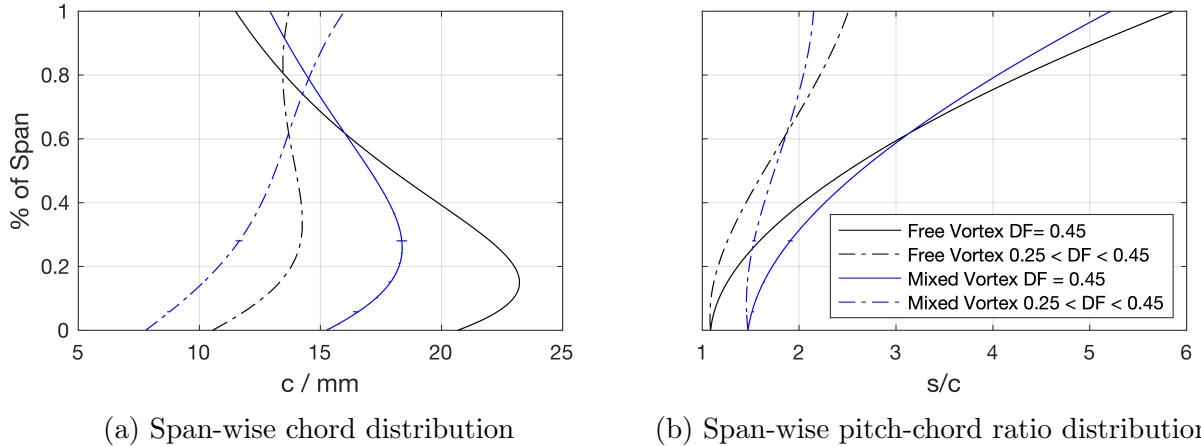


Figure 3.7: Span-wise distributions are shown for both the free and mixed vortex conditions (black and blue lines respectively) at both constant diffusion factor and linearly varying diffusion factor

Using the blade number the local chord can be determined using local pitch-chord ratio and radius such that

$$c = \frac{2\pi r}{(s/c)N} \quad (3.43)$$

The resulting span-wise chord distribution from both the free and mixed vortex conditions are shown for the rotor blade in Fig. 3.7a (solid line). For the free vortex condition it shows the variation in chord across the span to be large with tip chord less than half the maximum chord. Changing to the mixed vortex condition reduces this variation significantly with both the tip chord increasing and the hub chord decreasing. The variation in the free vortex design arises from Eqn. 3.40 as the range of velocities across the span result in large variations in pitch-chord ratio (as in Fig. 3.7b). Lieblein *et al.* (1953)^[10] shows an increase in loss for diffusion factors above 0.55 in the hub to mean-line regions, and 0.3 in the tip region. Therefore varying the diffusion factor across the span maintains a constant margin to Lieblein's suggested limits. The dot-dashed lines in Fig. 3.7b show the same vortex distributions as the solid lines but with the diffusion factor varying linearly from 0.45 at the hub to 0.25 at the tip. This limits the variation in pitch-chord ratio across the span. Consistency in pitch-chord has further implications for deviation and is explored in the following section.

3.3.5 Deviation

Flow deviation is estimated from correlations proposed by Howell (1945)^[12], (1945)^[13], and Carter (1950)^[14]. Commonly referred to as Carter's rule it states that for a compressor blade

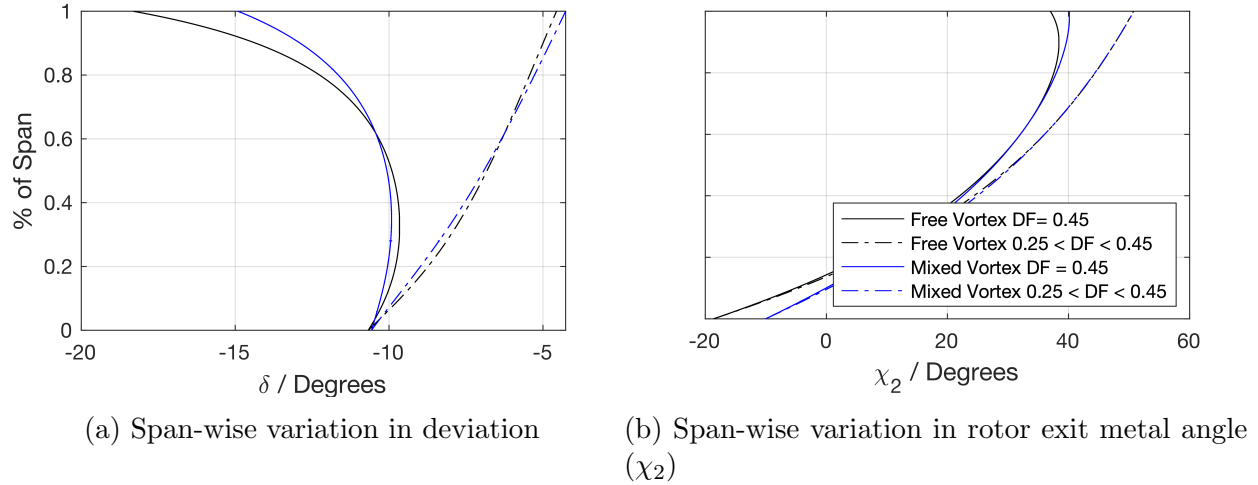


Figure 3.8: Span-wise distributions are shown for both the free and mixed vortex conditions (black and blue lines respectively) at both constant diffusion factor and linearly varying diffusion factor

$$\delta = m\theta \sqrt{\frac{s}{c}} \quad (3.44)$$

where θ is the flow turning achieved in the relative frame, and m is an empirically determined variable that can be approximated by

$$m = 0.23 \left(\frac{2a}{l} \right)^2 + \frac{\beta_2}{500} \quad (3.45)$$

where for a circular arc camber line $a/l = 0.5$. Hence the deviation varies $\sim \sqrt{s/c}$. Figure 3.8a shows the large increase in deviation angle at the rotor tips for both the free and the mixed vortex conditions when a constant diffusion factor is used (solid lines). Introducing a varying diffusion factor (dot-dashed lines) across the span reduces this deviation as the pitch-chord ratio varies less (Fig. 3.7b). Carter's rule is derived from empirical results obtained from compressor cascades (hub-tip ratio ≈ 1), and as such care must be taken when applying it to blades with large span-wise variations in pitch-chord ratio. A varying diffusion factor reduces the range of pitch-chord ratio significantly and Carter's rule predicts lower deviation angles. Consequently the variation in rotor exit metal angle is more consistent, as in Fig. 3.8b.

3.3.6 Blade Lean

Taylor & Miller (2016)^[15] shows the limits of using a 2-dimensional design with respect to 3-dimensional flow. Ensuring the blade suction surface subtends the hub and casing at an obtuse angle helps reduce corner separations and trailing edge losses. Lean is added to the

rotor and stator blades to satisfy this requirement. The rotor has 10° of lean at the hub and approximately 40° at the tip and the stator follows a parabolic lean profile with 10° of lean at the hub and tip.

3.3.7 Noise

Similar blade numbers in the rotor and stator or low common multiples of blade number results in more blade interaction and higher acoustic dB. Odd or prime numbers are selected to minimise interaction, provided this number is not too far from the calculated required blade count. Table 3.3 shows this process for each vortex design.

3.3.8 Blade Profiles

Low Reynolds number blade profiles were obtained from Maffioli *et al.* (2015)^[7]. The profile is designed for $Re \approx 5 \times 10^4$.

3.3.9 Blade Generation

The design flowchart in Fig. 3.1 is constructed in a MATLAB design environment to produce blade profiles as *.ibl files that are imported into a CAD package to begin the propulsor mechanical design.

4 Electrical and Mechanical Design

4.1 Introduction

With the propulsor design specified the electrical and mechanical design must be considered. The electric motor and corresponding power supply is chosen to be compatible with both the propulsor aerodynamic design and the system control and instrumentation architecture.

4.2 Electrical Design

4.2.1 Motor Requirements

Required motor speed is 6000 RPM giving a required isentropic power of 54.4 W. The shaft torque required is therefore $\tau_s = 0.0867\text{Nm}$. This is the torque required for isentropic flow assuming no windage and electrical losses from the motor, or other frictional losses. The delay between a vehicle disturbance and the motors responding to this disturbance, known as the control latency, should also be minimised to increase stability. Reducing the control latency also reduces data noise when conducting hover tests as the power requirement from the motors is more stable. Therefore, the motors must possess sufficient torque to rapidly respond to the control system. The moment of inertia of the rotor about its rotation axis is $I_{ZZ} = 51.01\text{kg} \cdot \text{mm}^2$ from a mass analysis of a CAD model of the rotor. The angular acceleration of the rotor is given by

$$I_{ZZ}\dot{\Omega} + \frac{\tau_s}{\eta_a} = \tau_m \quad (4.1)$$

where η_a is the aerodynamic efficiency. Taking τ_s as constant and equal to the value obtained above, the required motor torque, τ_m for a given angular acceleration of the shaft is equal to

$$\tau_m = 51.01 \times 10^{-6} \cdot \dot{\Omega} + \frac{0.0867}{\eta_a} \quad (4.2)$$

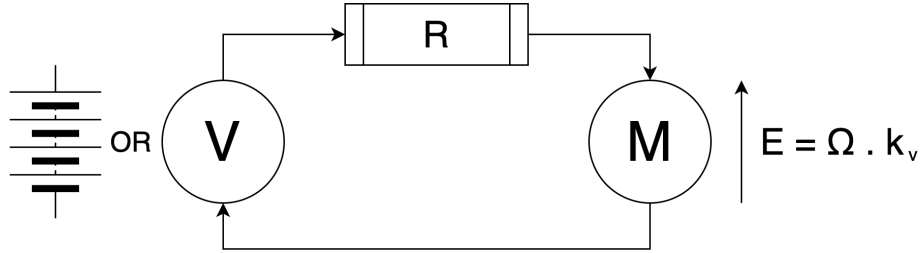


Figure 4.1: Electric motor model for DC/BLDC motors

4.2.2 Power Supply

A 12V/84A (1kW) DC power supply is used to power the stationary propulsor tests and can be used in conjunction with a tether to provide flight power for hover tests. The flying test bed is also equipped to hold a 4-cell Li-Po with a nominal voltage of 14.8V to enable future dynamic testing. The 12V power supply is used to determine the motor requirements as it is the limiting factor.

4.2.3 Choice of Electric Motor

A brushless DC motor (BLDCM) is modelled by the circuit in Fig. 4.1. The back-emf generated by the motor is proportional to the motor speed (as in Fig. 4.1) and the torque produced is proportional to the current. Given that the torque constant, k_t , and emf constant, k_v , are related by $k_t = 1/k_v \implies \tau_m = 3k_t I_{phase} = \frac{\sqrt{3}I_{supply}}{k_v}$. The motor speed can be related to the electrical input quantities by

$$V = IR + E \implies V = \left(\frac{\tau_m k_v}{\sqrt{3}} \right) R + \Omega k_v \quad (4.3)$$

$$\therefore \Omega = \left(V - \frac{\tau_m k_v}{\sqrt{3}} R \right) \cdot k_v \quad (4.4)$$

Assuming linear acceleration from rest to demand speed ($\dot{\Omega}_{max}$) and a maximum acceleration time of 75ms, Eqn. 4.2 gives a maximum motor torque requirement of $\tau_m =$

$0.428 + 0.0867/\eta_a$ Nm. The motor is required to have an outer diameter no greater than $30mm$ to fit inside the hub with hub wall thickness of $5mm$. These requirements, are met by a Multistar Elite 2810-750kv BLDCM with internal resistance of 0.108 ohms and emf constant of $750 \text{ RPM} \cdot \text{V}^{-1}$. Rearranging Eqn. 4.4 gives an output torque at 6000 RPM:

$$\tau_m = 0.76 \text{Nm} \quad (4.5)$$

This enables a maximum acceleration of $\dot{\Omega}_{max} = 8400 \text{ rad}\cdot\text{s}^{-2}$ given an aerodynamic efficiency $\eta_a > 30\%$.

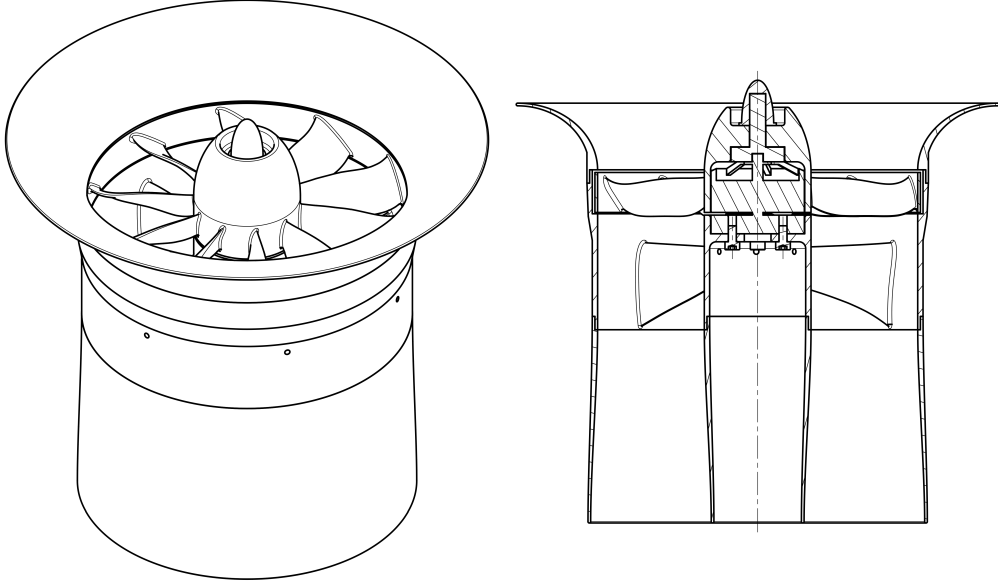


Figure 4.2: Isometric and section view of ducted fan design

4.3 Mechanical Design

In this section the propulsor design is embodied and the mechanical aspects of the design considered. The propulsors positioned diagonally opposite from each other spin in one sense and those on the other diagonal spin in the other sense. This gives the flying test bed yaw control. As a result two versions of the propulsor are produced, one spinning clockwise and the other anti-clockwise. These are simple mirror images of each other and so need not be discussed further.

4.3.1 Propulsor Dimensions

The rotor and stator profiles determined in Section 3.3 have a total axial chord of $52.5mm$ including a $12mm$ blade row gap. A blade duct length of $L = 60mm$ is chosen. Equation 3.12 gives values of $(r_c)_{exit} = 62.6mm$ and $(r_h)_{exit} = 17.4mm$. Table 3.4 shows the

values of the remaining geometric variables. Figure 4.2 shows the embodiment of this design. The propulsor is modular allowing for quick part replacement and is comprised of 5 aerodynamic components and 1 electric motor (including rotor mount and spinner). The assembled propulsor has a length of 167mm and a maximum diameter (at the intake) of 180mm. Design considerations for each component are discussed below.

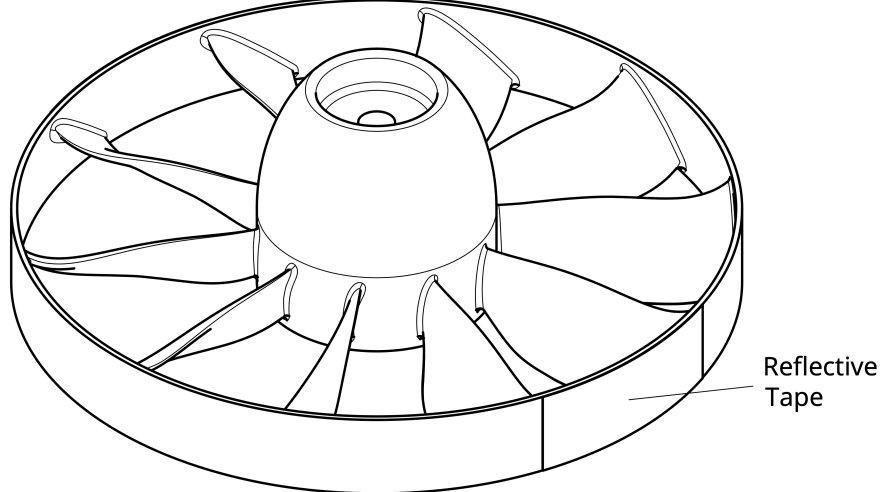


Figure 4.3: Isometric view of shrouded rotor

4.3.2 Shrouded Rotor

The rotor has 11 blades and is shrouded as in Fig. 4.3. The shrouding provides support for 3D printing to enable large overhangs without the blades deforming. The amount of support material required is minimised as it can adversely affect the surface finish of the blades. Reflective aluminium tape is fixed to the outside of the shroud and coupled with an IR photo-transistor mounted to the casing to enable measurement of rotor speed. The clearances required to ensure the shroud does not rub against the casing means the tip-gap required is large, $\approx 5\%$ of span, which introduces shroud clearance flow losses. Corner separations at the blade-shroud interface are minimised by adding lean to the blade as described in Section 3.3.6. To maintain a high quality printing finish on the trailing edge of the blade, print support should be avoided and so the blade is shifted in the axial direction to minimise the distance between the trailing edge and the build plate, located on a $r-\theta$ plane on the downstream side of the rotor. Maximum stress is expected at the blade-hub interface and so a fillet of 0.75mm is added to limit stress concentrations. A finite element analysis (FEA) of the rotor at operating speed is undertaken. The rotor is fixed at the motor shaft and a centrifugal force is applied with equivalent rotor speed of 6000 RPM. A total force of 3.47 N is distributed across the blades to simulate the thrust generated by the blades. This corresponds to 58.6% of the total thrust generated, as shown by Barry (2019)^[16]. 1st Order elements are used and the local mesh size at the blade hub is set to $\approx 0.1\text{mm}$. The von Mises yield criteria can be expressed as

$$\sigma_{yld} = \sqrt{3}k_{PLA} \quad (4.6)$$

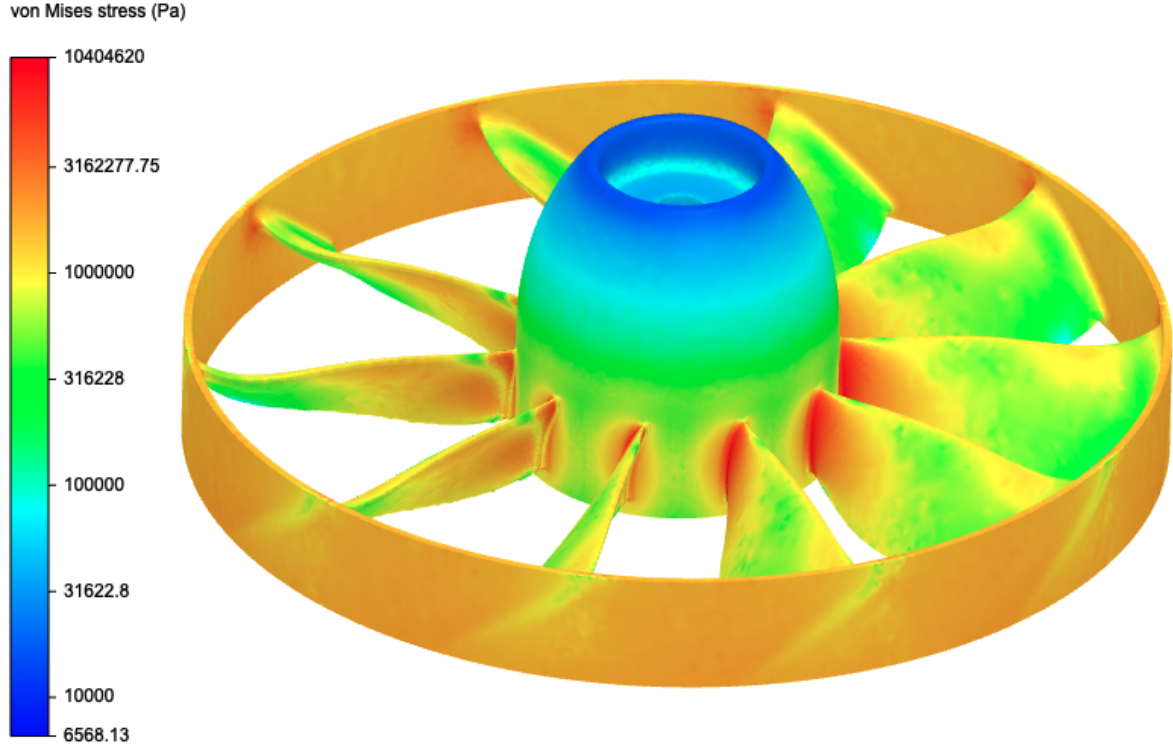


Figure 4.4: Finite element analysis of the rotor at operating speed with color bar showing von Mises stress with a logarithmic scale

where $k_{PLA} = 33$ MPa is the shear yield strength of 3D printed PLA as found by Anderson (2017)^[17]. This gives a maximum von Mises stress of $\sigma_{yld} = 57.2$ MPa. The FEA results in Fig. 4.4 show the maximum von Mises stress to be $\sigma_{vm} = 10.4$ MPa giving a yield margin of safety of 4.5. Radial displacement is negligible and so shroud clearance to casing is governed by tolerances required for shroud eccentricity as a result of 3D printing. The shroud has a thickness of 1mm and there is a 2mm gap between the rotating shroud and the stationary casing.

4.3.3 Stator Block: Stator Blades, Casing, and Hub

The stator blades, casing, and hub are one 3D printed part as shown in Fig. 4.5. The blades are both aerodynamic and structural components. The stators transfer the force of the fan to the drone chassis via the casing and arm. The electric motor mounts to part of the hub known as the mounting plate with 4 x M3x6 cap-head bolts. The plate has ventilation holes that match the underside of the motor to allow airflow to cool the motor and prevent overheating. Although the motor is operating at 20% rated power, maintaining airflow prevents the PLA expanding during operation which can cause warping or rubbing.

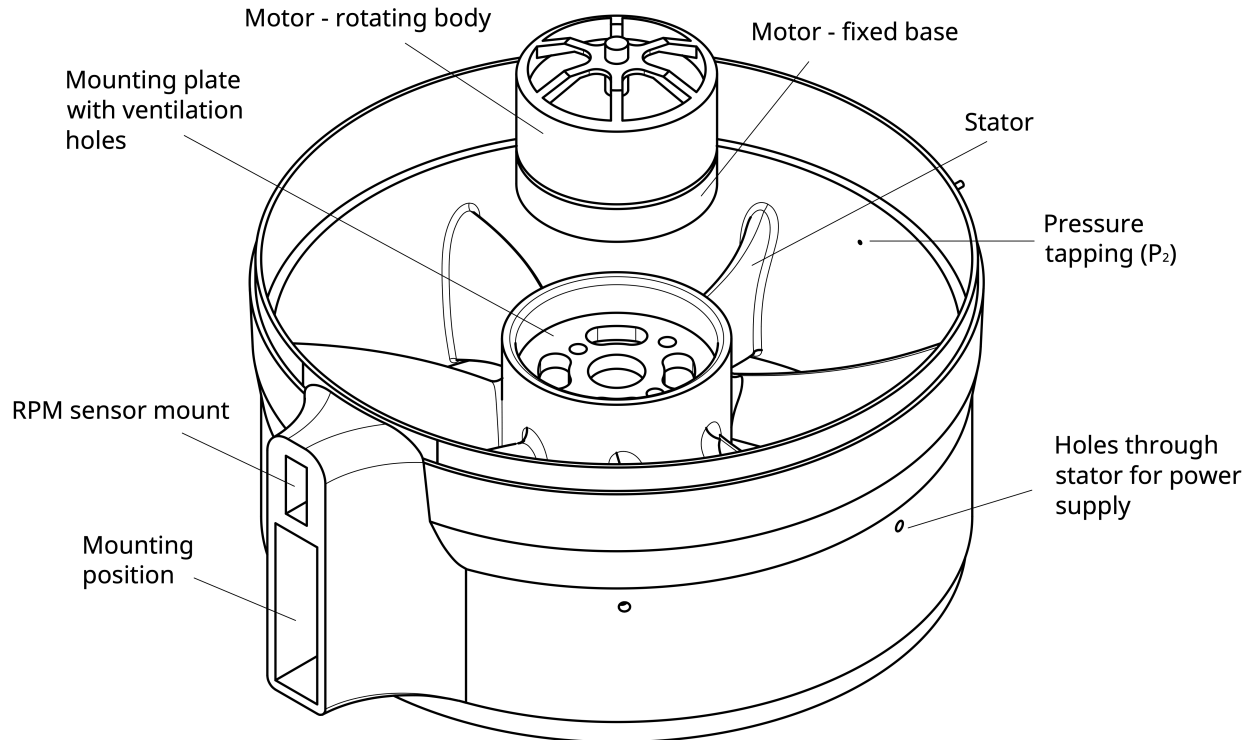


Figure 4.5: Exploded view of stator block and electric motor

The ventilation holes also allow the 3 power wires on the motor into the hub cavity below the mounting plate where they are connected to three power supply cables. These power cables are fed from the flying test bed through passages in the stator blades that can be seen as holes on the casing in Fig. 4.5. These passages are generated by outputting the line of maximum blade thickness and lofting a circular section along it. The 3D printer generates minimum wall thicknesses of approximately $0.3mm$ so to avoid the passage breaking through the stator wall the loft diameter is less than the maximum stator thickness minus $2 \times 0.3mm$. At the hub the maximum thickness is $2.15mm$ therefore the maximum passage width is $2.15 - 2(0.3) = 1.55mm$. This sets the limit for power supply wire thickness. The hub provides an interference fit to the motor to reduce rotor eccentricity with respect to the casing. The intake and diffuser sections also mount to the stator block with an interference fit. Both intake and diffuser casing are fixed in place with adhesive tape. The mounting point for the propulsor to be attached to the flying test bed or the stationary test rig is sized to the outer dimensions of the load-cell. The arm attachment is shaped like the load-cell so the same mounting point can be used.

4.3.4 Diffuser

The diffuser is mounted to the stator block via an interference fit. The casing is also held in place with adhesive tape as it is more prone to detaching under vibration than the hub.

Both diffuser hub and casing are designed to be as thin as possible while remaining rigid. At exit the diffuser has a thickness of $1mm$ and at entry it has a thickness of $2mm$.

4.3.5 Intake

The intake is mounted to the stator block via an interference fit. As it generates thrust it must be securely attached to the stator block and so adhesive tape is also used. The intake is less prone to eccentricity as it has a curved cross-section. It can be printed with a constant thickness of $1mm$. Print times for the intake can be large (> 1 day) as significant support material is required due to the overhang of the lip.

4.3.6 3D Printing

All structural and aerodynamic parts are made using an Ultimaker 3 3D printer and $2mm$ diameter RS Pro PLA filament. Prints have 75% infill with a cubic subdivision pattern.

5 Experimental Methods

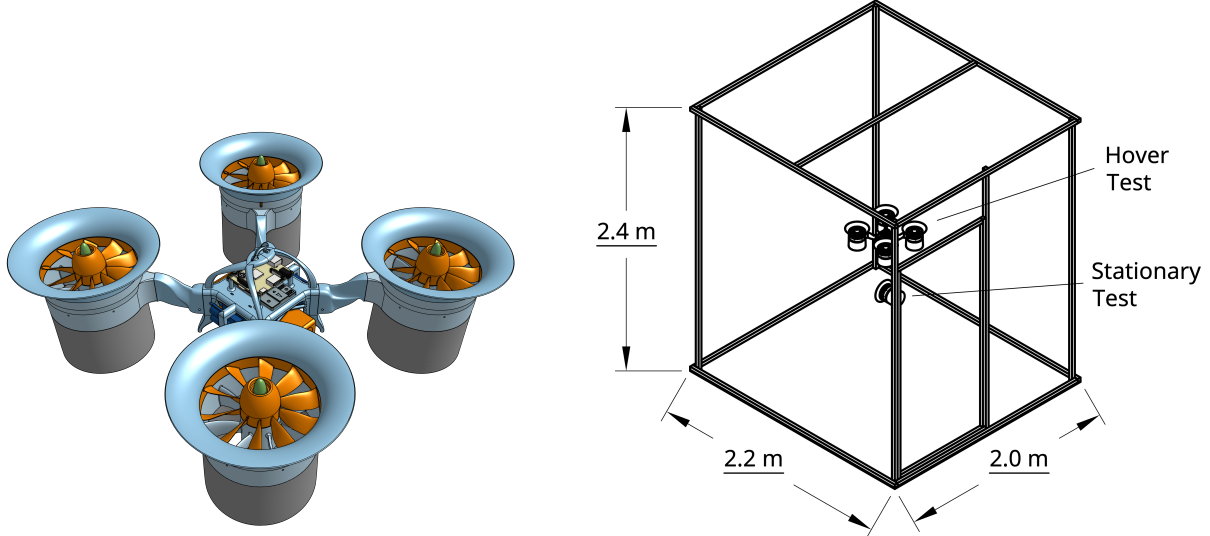
Two types of experiment are undertaken: stationary propulsor tests and hover tests to determine system performance. All testing is done in a purpose built indoor test environment at the Whittle Laboratory. Figure 5.1b shows the cage constructed to provide protection from the propulsor and flying test bed. A retrospective risk assessment analysis is conducted in Appendix B. Figure 5.1a shows a render of the flying test bed with ducted fans mounted for hover tests.

5.1 Cage Design & Tether

Figure 5.1b shows the safe indoor test environment constructed for conducting both stationary propulsor and hover tests. The $2.0m \times 2.2m \times 2.5m$ frame is constructed out of $3cm \times 3cm$ section timber beam. An inward opening door provides access to the environment and is hung so that it closes automatically for safety. $1cm$ grid chicken wire walls are fastened securely on each beam. The wire is in tension to increase the frame's rigidity. A central beam crosses the top of the cage and acts as the mounting point for the tether. $1m$ of shock cord is attached to a long piece of parachute cord using a carabiner. The parachute cord is fed over the central beam on the top of the cage and over the cage edge above the door allowing the tether to be raised or lowered from outside of the cage.

5.2 Stationary Propulsor Test

Propulsor performance is tested on the stationary test rig, shown in Fig. 5.2, to determine thrust, power, RPM, and motor temperature as well as characterise the aerodynamic performance with static pressure measurements. All electronic connections are made using metallic



(a) Perspective render of flying test bed in hover test configuration

(b) Test cage shown in isometric view with flying test bed in hover test configuration and an individual propulsor in the stationary test position (stationary test mount not shown)

braid shielded cable. Thrust, power, and RPM data is collected by the flying test bed chassis and the main motor outputs are used to power and control the propulsor. Temperature readings are made using an external thermometer.

5.2.1 Setup

Figure 5.2 shows the experimental setup for stationary tests in the calibration configuration. An aluminium speed-frame structure is fixed to the ground and has a horizontal mounting beam 1m in height and 1m in length. Thrust, RPM, temperature and pressure measurements require external sensors; their setup is described below. The flying test bed requirements for stationary testing is also described.

Load-cell The propulsor is mounted at one end of the frame via a 0.6kg rated single ended shear beam load-cell mounted perpendicular to the axis of the fan. A low friction pulley is mounted to the other end of the frame with the top of the pulley in line with the axis of the fan. Light-weight high tensile fishing wire is attached to the rotor spinner and is fed over the pulley, attaching to a vertically hanging weight that is used to calibrate the load-cell. This weight can be varied in multiples of 50g up to 500g. When testing, the wire is detached from the spinner and secured so as not to interfere with the fan. The load-cell connects through an HX711 ADC/amplifier breakout board that is mounted to the frame. Data is transmitted from the HX711 to the GPIO pins of the RPi3.

IR Photo-transistor The IR photo-transistor inserts into an interference fitted slot above

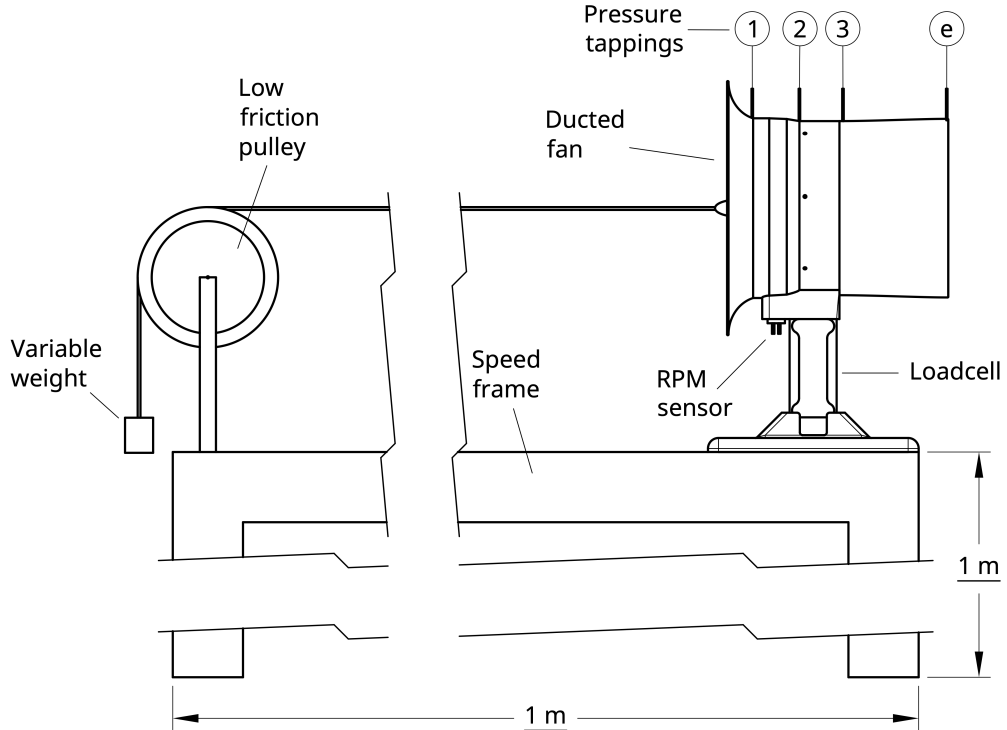


Figure 5.2: Experimental setup of stationary tests in calibration configuration

the mounting point, as in Fig. 5.2. A potential divider circuit is connected to the output of the photo-transistor and is connected to the 5V DC/Ground and GPIO pins of the RPi3 via the shielded cable.

Thermocouple The K-type thermocouple is fixed with super glue to the motor mounting plate in the propulsor hub with the sensing junction resting against the base of the motor. The other end is fed through a hollow stator and is plugged into a K-type thermocouple external thermometer from which temperature readings are taken.

Pressure Transducers 1.1mm holes are drilled radially into the casing at 4 axial locations as in Fig. 5.2: p_1 upstream of the rotor; p_2 upstream of the stator; p_3 downstream of the stator; p_e exit from exit duct. 1.1mm outer diameter hypodermic tube tappings are inserted into the holes and secured with super glue on the outside of the casing, ensuring the tapping does not protrude into the flow on the duct side of the casing. Plastic tubing with 1mm inner diameter is fixed to the end of the tappings and connected to input ports of a 16-channel external pressure transducer DSA. The DSA is connected via an ethernet switch to the control station from which gauge pressures (relative to ambient) can be read. The DSA is positioned over 1m away from the propulsor in the $r\theta$ plane to reduce the impact of the propulsor on the measured ambient pressure.

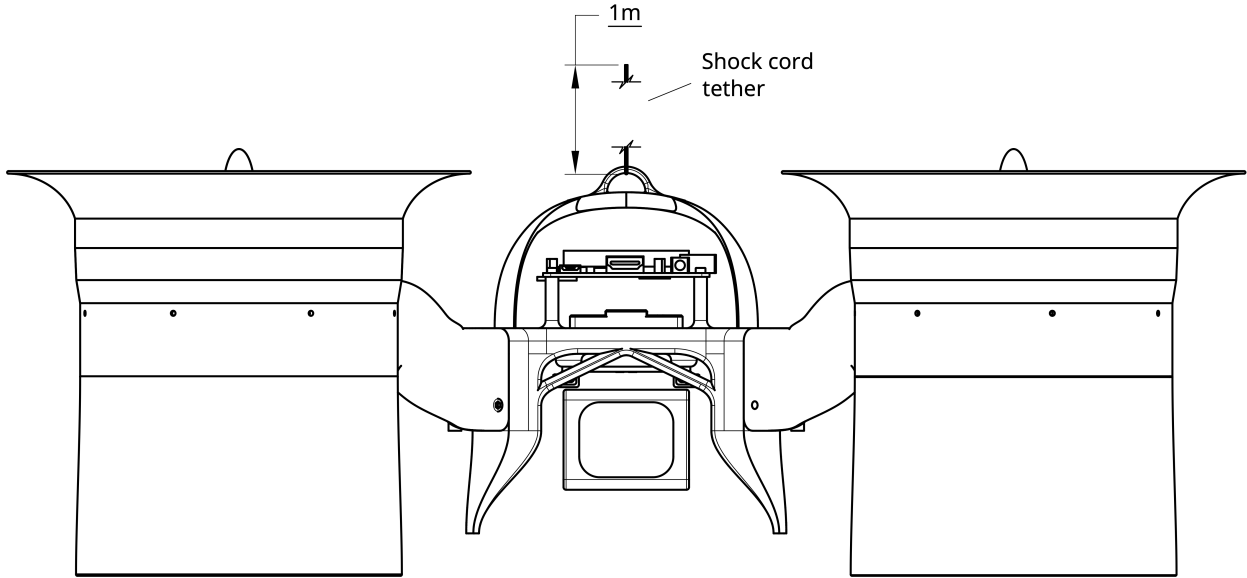


Figure 5.3: Front view of flying test bed in hover configuration

5.3 Hover Test

Hover tests are undertaken in the test environment by mounting propulsors to the flying test bed and conducting a static hover from a top-down tether. The hover test determines the figure of merit in flight by calculating the power required and equating vehicle weight to thrust. Vehicle stability in hover is also considered qualitatively. The propeller results allow the performance in flight to be compared to stationary tests. Further methods of testing are discussed in Section 7 on Future Work.

5.3.1 Setup

The tether ensures the flying test bed is clear of the ground to reduce any ground effect. The tether is made of 1m of shock cord (slack) to reduce stress on the structure in the event of a sudden loss in power or emergency situation in which the propulsors must be shutdown. To attach the tether to the flying test bed and act as a roll cage in the event of a collision with the topside of the chassis, an arched frame can be mounted to the chassis as in Fig. 5.3.

5.3.2 Control

The Pixhawk 4 flight controller altitude hold mode attempts to maintain the current altitude and position using its onboard GPS, accelerometers, and gyros. The indoor test environment reduces the GPS accuracy and so manual corrections are made using a handheld radio transmitter. Automatic position holding is possible using the forward-right-down ultrasound sensor array.

5.4 Measurement Techniques

Measurements are taken to determine the overall performance in terms of the figure of merit, power and thrust, and aerodynamic performance in terms of pressure coefficients, flow coefficient and stage loading and noise levels produced by different propulsors. All measurements are taken after 5 minutes of continuous operation to reduce transient temperature effects in the motor and electronics.

5.4.1 Non-dimensional Quantities

Figure of Merit Figure of merit is found using measured or equivalent thrust and electrical power required. Thrust is measured directly using the load-cell in the stationary tests but in the hover tests the thrust is taken as being equal to the flying test bed mass, which is measured prior to flight using a high precision scale. Both load-cell and scales have an accuracy of $\pm 0.1\text{g} \approx \pm 0.1\text{mN}$. Power is measured as electrical power output from the Pixhawk 4. Readings are accurate but due to noise, particularly during hover tests, they can be imprecise. Taking a mean value over a large window reduces the effect of noise. The flow area is assumed as designed ($A_x = \pi(r_c^2 - r_h^2)$) and air density is calculated from ambient temperature and pressure.

Flow Coefficient Flow is assumed axial at inlet and stagnation pressure equal to atmospheric pressure. Using Bernoulli's equation the axial flow velocity at the casing is determined and the flow coefficient evaluated by dividing by the local blade speed, as in Eqn. 5.2. Taking the span-wise distribution of flow coefficient to be equal to that determined in Section 3.3.1 the mean-line flow coefficient can be determined from Eqn. 3.27a

$$\phi = \phi_m \left(\frac{r}{r_m} \right)^A \implies \phi_m = \phi_c \left(\frac{r_c}{r_m} \right)^{-A} \quad (5.1)$$

$$\therefore \phi_m \approx \left(\frac{V_x}{U} \right)_c \cdot \left(\frac{r_c}{r_m} \right)^{-A} \implies \phi_m \approx \sqrt{\frac{(p_a - p_1)_c}{\frac{1}{2}\rho(\Omega r_c)^2}} \cdot \left(\frac{r_c}{r_m} \right)^{-A} \quad (5.2)$$

Static pressure p_1 is measured as gauge pressure relative to atmospheric, $p_1 - p_a$. Rotor RPM is measured using the IR photo-transistor. Casing and mean-line radius are taken as their design values.

Stage Loading Stage loading can be estimated by assuming the exit flow from the stator is axial as well as $\partial V_x / \partial x = 0$ due to incompressibility and negligible radial velocity. Using Bernoulli the static pressure at stator exit, p_3 , can be related to the change in stagnation pressure as follows

$$\Delta p_0 = p_{03} - p_{01} \implies (p_3 + \frac{1}{2}\rho V_x^2) - p_{01} \xrightarrow{p_a} \quad (5.3)$$

From Eqn. 3.2 stage loading can be written in terms of Δp_0 and so substituting Eqn. 5.3 gives

$$\psi = \frac{p_3 - p_a}{\rho U^2} + \frac{1}{2} \left(\frac{V_x}{U} \right)^2 \quad (5.4)$$

where $p_3 - p_a$ is the measured gauge static pressure. A similar expression to Eqn. 5.2 can be found for stage loading and so the mean-line stage loading can be estimated by

$$\therefore \psi_c = \frac{(p_3 - p_a)_c}{\rho(\Omega r_c)^2} + \frac{1}{2} \phi_c^2 \implies \psi_m \approx \left[\frac{(p_3 - p_a)_c}{\rho(\Omega r_c)^2} + \frac{1}{2} \phi_c^2 \right] \cdot \left(\frac{r_c}{r_m} \right)^{-B} \quad (5.5)$$

Diffuser Static Pressure Recovery Equation 3.9 shows the theoretical static pressure recovery coefficient can be expressed in terms of the exit duct area ratio, σ . Assuming V_x remains constant this is written in terms of the measured static pressures

$$C_{pr} = \frac{p_e - p_3}{\frac{1}{2} \rho V_x^2} = \frac{p_e - p_3}{p_a - p_1} \quad (5.6)$$

Thrust Coefficient Thrust output is non-dimensionalised by mean-line blade speed and flow area, as in Eqn. 5.7

$$C_T = \frac{T}{\frac{1}{2} \rho (\Omega r_m)^2 \cdot A_x} \quad (5.7)$$

Mean-line blade speed is calculated from the recorded RPM and the design mean-line radius.

5.4.2 Data Acquisition and Processing

In this section, methods for recording and processing the data streams of thrust, power, RPM, pressure, and temperature are described. Data is collected for ≈ 30 seconds and mean values are obtained for each data stream. Mean values are used in the analysis and time-sampled data is verified to be steady.

Thrust Prior to each test the load-cell is tared to remove any zero error. The load cell is then calibrated in order to determine the thrust developed by the propulsor using the setup in Fig. 5.2. A Python script on the RPi3 records thrust from load-cell measurements (simultaneously with RPM) and data is wirelessly imported to MATLAB via the SCP protocol. Raw values are compared to the fit obtained during calibration to determine the corresponding thrust. The mean thrust is determined.

Power Power is measured by recording the output DC voltage and current from the PM07 power management board. The maximum sample rate is $\approx 1Hz$, limited by the telemetry data transmission protocol, and so ≈ 30 readings are made. Voltage and current data is obtained through the logging feature on QGroundControl: MavLink Inspector via the

telemetry module. The recorded log is automatically imported into MATLAB for processing. Instantaneous samples of current and voltage are multiplied to determine instantaneous power. A mean power is then determined.

RPM At operating speeds the required IR photo-transistor sample rate to reliably determine RPM is 16 kHz. The RPi3 was found to have a GPIO sample rate of 30 kHz therefore recording RPM from 2 propulsors would require a sample rate above this. Assuming negligible variation in electric motor and propulsor performance, all 4 propulsors should operate at a similar RPM during static hover and so one RPM reading is sufficient to determine mean rotor speed. A Python script on the RPi3 records RPM from the IR photo-transistor (simultaneously with thrust) and data is wirelessly imported to MATLAB via the SCP protocol. RPM is determined by timing how long it takes for consecutive reflective strips to be registered. RPM is calculated by averaging the rotation period over 10 rotations. This reduces the error as the sample location on the leading edge of the reflective strip varies.

Pressure Pressure tappings measure static pressure at the casing. Flow quantities such as flow coefficient are determined at the casing and their mean-line values are estimated from the design span-wise distributions. Pressure is measured from the DSA as gauge pressure relative to atmospheric, $p - p_a$, taking ≈ 100 readings over 30 seconds. Each reading is made up of 1000 instantaneous samples. Measurements are made simultaneously with thrust, power, RPM, and temperature measurements to synchronise the data and account for any transient behaviour. Data is recorded directly into MATLAB on the control station. Non-dimensional quantities are calculated as in Section 5.4.1. The mean is calculated over the 100 readings.

Temperature One K-type thermocouple is fixed to the mounting plate of the electric motor in the ducted fan hub. This is connected via a 1m long cable to a thermocouple thermometer. Whilst data is collected the temperature is monitored to ensure it remains below 50°C, well below the PLA glass transition temperature of 60 – 65°C. Temperature readings are made during the stationary tests but cannot be made during hover tests.

6 Results

6.1 Stationary Propulsor Test

Due to disruption caused by the Coronavirus pandemic (see Appendix A) three prototype ducted fans were tested; A, B, and C. Fan D was not tested. Before considering the ducted fans the electrical efficiency of the flying test bed system is determined. Second, the performance of two different intake designs are compared. Third, the figure of merit is used to analyse the relative performance of the three ducted fans. Finally, the mass model is analysed and the superiority condition evaluated.

6.1.1 System and Electrical Efficiency

System electrical efficiency is estimated by comparing experimental data for the APC propeller to the manufacturer's calibration data^[18]. The shaft figure of merit, defined using the power at the shaft, $P_s = \Omega \cdot \tau_s$, is determined from the calibration data. Assuming any aerodynamic losses are incurred equally by both experiment and calibration data, the difference in figure of merit can be accounted for by the electrical efficiency of the flying test bed system, known hereafter as the system efficiency, $\eta_{sys.}$. This is found by the ratio of the experimental to the calibration data figure of merit:

$$\eta_{sys.} = \frac{M_{F,exp.}}{M_{F,cal.}} \quad (6.1)$$

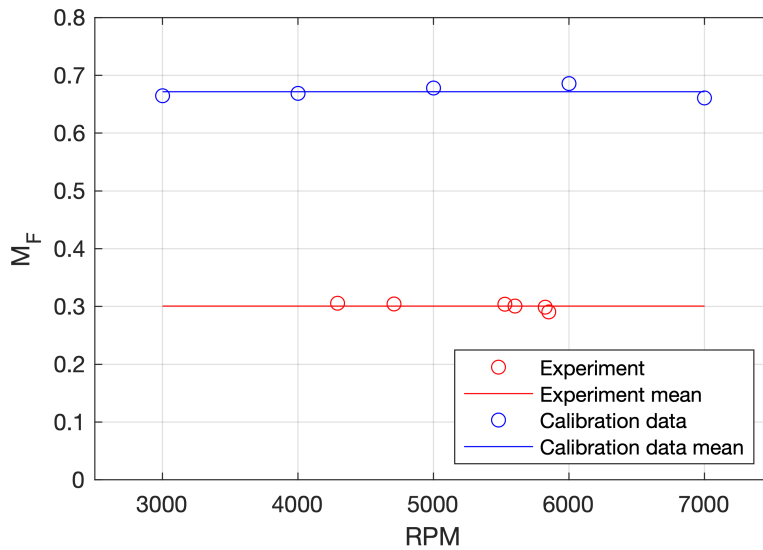


Figure 6.1: Figure of merit for APC propeller from experiment and calibration data

Figure 6.1 shows the figure of merit determined for the APC propeller from the stationary propulsor test and calibration data to vary with RPM by less than 4% and so the system efficiency is assumed constant. The system efficiency is calculated using the mean values from each data-set and is found to be

$$\eta_{sys.} = \frac{0.301}{0.672} = 45\% \quad (6.2)$$

This is used to estimate the shaft figure of merit of any propulsor tested on the stationary test rig.

6.1.2 Intake Performance

The two intake designs compared are shown in Fig. 6.2. The short intake produces audibly separated flow, as in Hubbard (1950)^[19], as the sound pitch and amplitude generated by the

fan increased. It is hypothesised that this is due to flow separation at the intake causing either part or full circumference tip stall. No significant variation in tone is observed with the long intake. The figure of merit of the long intake was found to be 30% higher than the short intake thus supporting these observations. The long intake was used in all other tests described here.

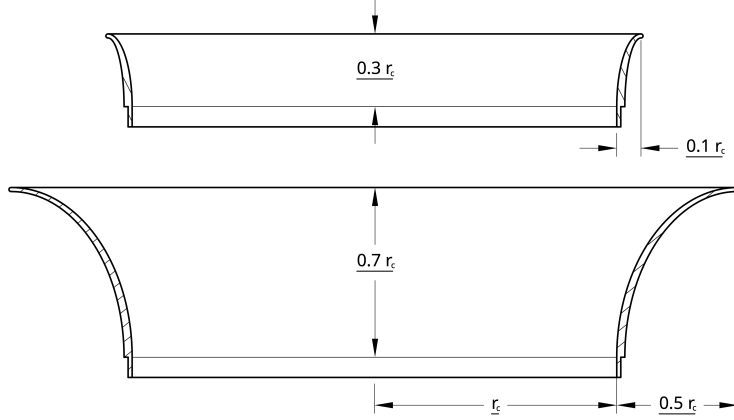


Figure 6.2: Dimensions of short and long intake

6.1.3 Ducted Fan Figure of Merit

Three prototype ducted fans were tested. Fan A has a constant angle vortex distribution whereas fans B and C are free vortex designs. Fan D is a mixed vortex design but was not tested. Fan D used a higher quality 3D printer configuration than fan B but they are otherwise identical. Mean-line flow coefficient and stage loading are evaluated and used to find the equivalent exit duct area ratio, as in Eqn. 3.4. Diffuser static pressure recovery is determined for fans A and B. Recorded figure of merit and corrected shaft figure of merit are evaluated for fans A, B and C enabling an aerodynamic efficiency to be determined as:

$$\eta_a = \frac{M_{F,s}}{M_{F,max}} \quad (6.3)$$

where $M_{F,max}$ represents the theoretical maximum figure of merit given for a propeller as $M_{F,max} = 1$ and for a ducted fan with exit duct area ratio σ as $M_{F,max} = \sqrt{2\sigma}$. Ducted fans are shown to have a higher figure of merit than both the propeller in stationary testing and the theoretical maximum figure of merit for a propeller, $M_{F,max} = 1$. The calculated aerodynamic efficiencies rely on the 3rd party propeller calibration data. The high aerodynamic efficiencies determined may therefore be inaccurate, however their relative magnitudes can still be used to compare propulsor performance.

The sources of aerodynamic loss, and subsequent variation in figure of merit of the 3 tested fans, are hypothesised to come from 3 main sources. Firstly, profile loss due to flow

Fan	Design							Experiment						
	ϕ_m	ψ_m	σ	B	DF _m	N	M _{F,s}	ϕ_m	ψ_m	σ	C _{pr}	M _{F,exp.}	M _{F,s}	η_a
A	0.8	0.25	1.13	-1.1	0.45	7	1.51	0.79	0.29	1.08	0.073	0.52	1.17	0.78
B	0.8	0.25	1.13	-2.0	0.45	7	1.51	0.74	0.33	0.82	0.079	0.58	1.29	0.86
C	0.8	0.25	1.13	-2.0	0.45	7	1.51	-	-	-	-	0.61	1.36	0.90
D	0.8	0.25	1.13	-1.7	0.35	11	1.51	-	-	-	-	-	-	-
Prop.	-	-	-	-	-	-	-	-	-	-	-	0.30	0.67	0.67

Table 6.1: Stationary test design parameters and results

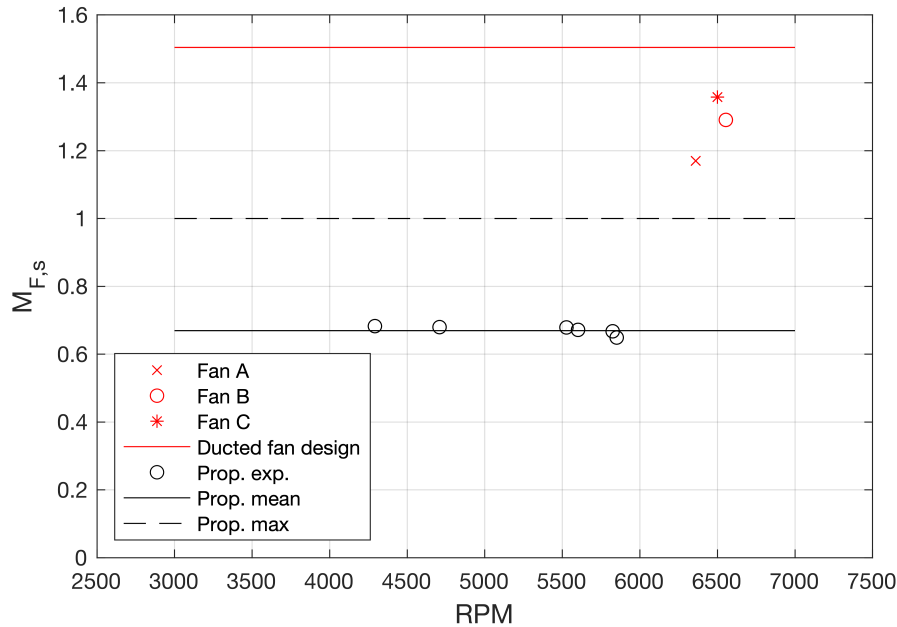


Figure 6.3: Corrected shaft figure of merit for ducted fans compared to propeller data

separation from the blade due to low Reynolds number effects and surface roughness. Secondly, tip loss due to shroud clearance flows and corner separation. Finally, manufacturing techniques introducing geometric deviation from design.

Profile Loss Fans A and B compare the performance of a constant angle vortex design ($B = -1.1$) and a free vortex design ($B = -2.0$). The two fans differ only in the rotor used. Table 6.1 shows the difference in efficiency between the two designs, and resulting difference in figure of merit. Lowering the vortex distribution exponent increases the blade chord at the casing adding more momentum to the boundary layer^[20]. This helps the flow remain attached to the casing and results in the experimentally obtained exit area ratio being higher for fan A ($\sigma_{exp.} = 1.08$) than fan B ($\sigma_{exp.} = 0.82$). This moves the operating point of fan B away from design, as shown by experimental ϕ_m and ψ_m in Table 6.1. The Smith chart in

Fig. 3.3a shows this operating point to have the same predicted aerodynamic efficiency as design of $\eta_a \approx 0.94$ and so the limited increase in profile loss is expected. Evaluating mean-line flow coefficient allows the variation in Reynolds number across the span to be estimated by assuming the flow coefficient distribution across the span is as designed. Reynolds number across the span of fan A varies from approximately 10,000 at the hub to 70,000 at the tip whereas fan B varies from 25,000 at the hub to 45,000 at the tip. It is hypothesised that the difference in $M_{F,s}$ between fan A and B is due to the low Reynolds number at the hub of fan A resulting in separation, as in Fig. 6.4, due to the Reynolds number being approximately 20% of the Maffioli blade profile design value.

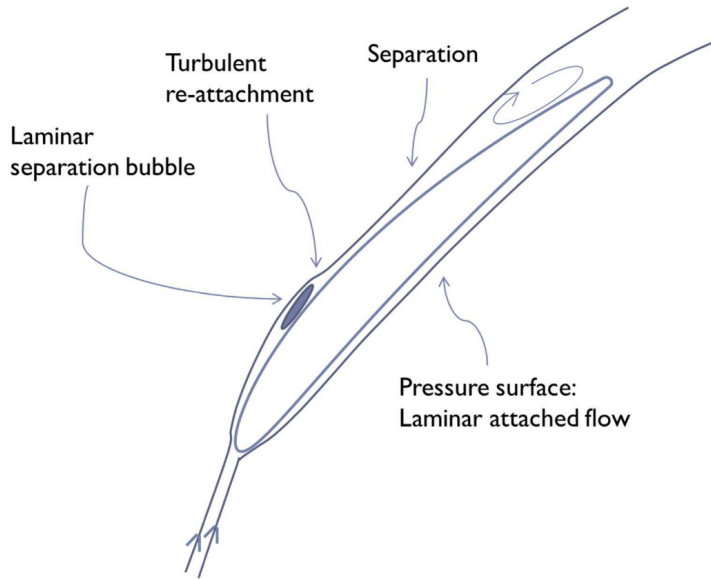


Figure 6.4: Typical boundary layer behaviour for low Reynolds number blade profiles in $\approx Re = 5 \times 10^4$ reproduced from Maffioli *et al.* (2015)^[7]

At the tip the Reynolds number is above the blade profile design value meaning the flow remains attached at the trailing edge resulting in minimal profile loss compared to the hub. This results in the flow coefficient and stage loading at the casing being as designed and so the evaluated flow coefficient and stage loading at mean-line is within 2% of the design values. This correlation with design is not expected to have been achieved at the hub due to separation. The Reynolds number at the hub of fan B is 50% lower than the blade profile design value but the hub chord is $\approx 200\%$ that of fan A and so less separation is expected to have occurred. The manufacturing process causes span-wise ridges on the surface of the blade as 3D printed layer thickness is finite, $0.1mm \approx 1\%$ of chord. This increases profile loss due to increased skin friction. This roughness could be reduced by printing the blades in a radial direction so that the ridges resulting from printing layers are in the direction of the flow. For this to be possible a 3D printer that uses a cylindrical coordinate system would need to be developed.

Leakage and End Wall Losses Denton (1993)^[21] describes a loss model due to mixing in shroud clearance flows. All flow angles are taken in the blade relative frame at the casing.

$$\frac{T\Delta s}{\frac{1}{2}V_2^2} = 2 \frac{m_l}{m_m} \left(1 - \frac{\tan \beta_1}{\tan \beta_2} \cdot \sin^2 \beta_2\right) \quad (6.4)$$

where the fractional leakage is given in terms of tip clearance, g , blade span, h , and rotor relative flow angles at the casing. The ratio of leakage mass flow to mainstream is given by

$$\frac{m_l}{m_m} = \frac{g}{h} \sqrt{\sec^2 \beta_2 - \tan^2 \beta_1} \quad (6.5)$$

For the design described in Section 3.3 this gives a loss coefficient of

$$\frac{T\Delta s}{\frac{1}{2}V_2^2} = 0.0093 \approx 1\% \quad (6.6)$$

This is a result of a shroud clearance of $\approx 2mm = 5\%$ of span. This clearance is required due to current manufacturing tolerances. Suggested manufacturing improvements are discussed below. Losses due to corner separation are reduced through the use of lean as in Section 3.3.6.

Diffuser Performance Diffuser performance is assessed assuming exit flow is straight and parallel. The coefficient of static pressure recovery across the diffusers of fan A and B is presented in Table 6.1. This shows the static-pressure recovery to be considerably lower than designed. Both fan A and B had a pressure tapping upstream (P_3) and downstream ($P_{diff,in.}$) of the joining line where the diffuser casing meets the stator block at the same design radius. Fan A and B manufacturing issues resulted in the trailing edge of the stator block being rough and slightly eccentric. The static pressure difference should be negligible between $P_{diff,in.}$ and P_3 however it is found that for both fan A and B the static pressure loss (normalised by flow velocity) is $P_{diff,in.} - P_3/0.5\rho V^2 \approx 0.1$. This suggests the flow separated at the joining line resulting in a loss in diffuser performance. The manufacturing issues experienced with fan A and B were resolved for fan C and so the increase in efficiency is attributed to improved diffuser performance resulting from improved manufacturing methods.

Manufacturing Process 3D printing the rotor blades introduces geometric deviations from the design in the form of surface roughness, large required clearances (both already discussed) but also warping and shrinkage. The FEA conducted in the design section shows the rotor geometry to have negligible deflection under load however as high temperatures are required during the 3D printing process, temperature gradients can be expected throughout the structure imparting thermal strain that can cause warping after cooling. The geometry of the printed part should be analysed using a 3D scanner and any geometric deviation quantified. Potential solutions to this problem include higher fidelity printing, ambient temperature regulation when printing, controlled cooling after printing, and annealing.

6.1.4 Ducted Fan Mass Model

Figure 6.5 shows the mass model predicted mass compared to the manufactured ducted fan mass. The model predicts the propulsor mass to within 14%, suggesting the mass model is valid at the scale considered here. The model does not consider wiring, the mass of mounting points, or fasteners. These account for the difference between the mass model and the actual mass of the propulsor. It should be noted that mechanical and structural considerations at larger fan diameters and higher thrusts may cause the model to deviate further from the manufactured propulsor, for example a thicker casing will be required at larger fan diameters to maintain structural rigidity. The choice of material and manufacturing method may change with size and application at which point the model may need updating, though the same modelling principles should still be valid.

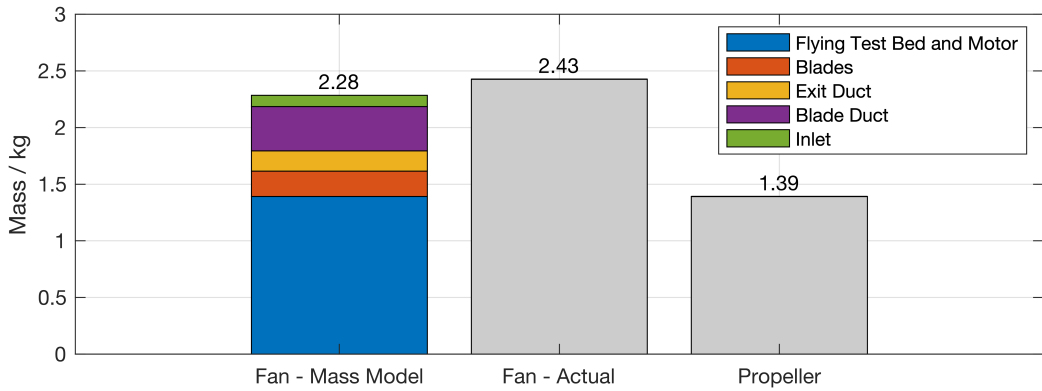


Figure 6.5: Comparison of flying test bed mass when driven by propellers or ducted fans. Mass model is compared to measured mass of vehicle for the ducted fan design

Considering the ducted fan performance criteria presented in Eqn. 1.13, the LHS of this inequality can now be determined.

$$\frac{W_{fan,total}}{W_{prop.,total}} = \frac{2.43}{1.39} = 1.75 \quad (6.7)$$

Showing that the ducted fan propulsors mounted to the flying test bed account for approximately 40% of the vehicle weight. This could be reduced through the use of advanced materials such as carbon composites to form a lightweight yet stiff casing structure. Assuming inlet, diffuser, hub and casing thickness can be halved, and taking the density of 61% carbon fibre reinforced plastic (CFRP) as $1600 \text{ kg}\cdot\text{m}^{-3}$ [22], the weight fraction reduces to

$$\frac{W_{fan,total}}{W_{prop.,total}} = \frac{2.01}{1.39} = 1.45 \quad (6.8)$$

6.1.5 Superiority Condition

Taking the superiority condition for a non-ideal propeller, Σ is expressed for the general case from Eqn. 1.14 as

$$\Sigma = \left[\frac{(M_{F,s})_{fan}^2 A_{x,fan}}{(M_{F,s})_{prop.}^2 A_{x,prop.}} \right]^{\frac{1}{3}} - \frac{W_{fan,total}}{W_{prop.,total}} \quad (6.9)$$

From experimental data for fan C, Eqn. 6.7, and the determined shaft figure of merit of the propeller, the superiority condition is determined:

$$\Sigma = 0.933 - 1.75 = -0.82 \quad (6.10)$$

Hence the superiority condition is not satisfied but superiority parameter Σ agrees with the design value to within 2%. As discussed in Section 3.2.6, the propulsor weight is too large with respect to the payload weight for the superiority condition to be satisfied. In a general application the propeller area and payload are not fixed and so the superiority condition may be satisfied. The area ratio between the propeller and the fan is given by $\Lambda = A_{x,fan}/A_{x,prop.}$, and the payload is W_P . Figure 6.6 shows how Σ varies across the Λ -payload design space when a CFRP construction is used and HTR is fixed at 0.2. Figure of merit for the fan and propeller are assumed equal to the experimentally obtained values for fan C and the propeller, 1.36 and 0.67 respectively.

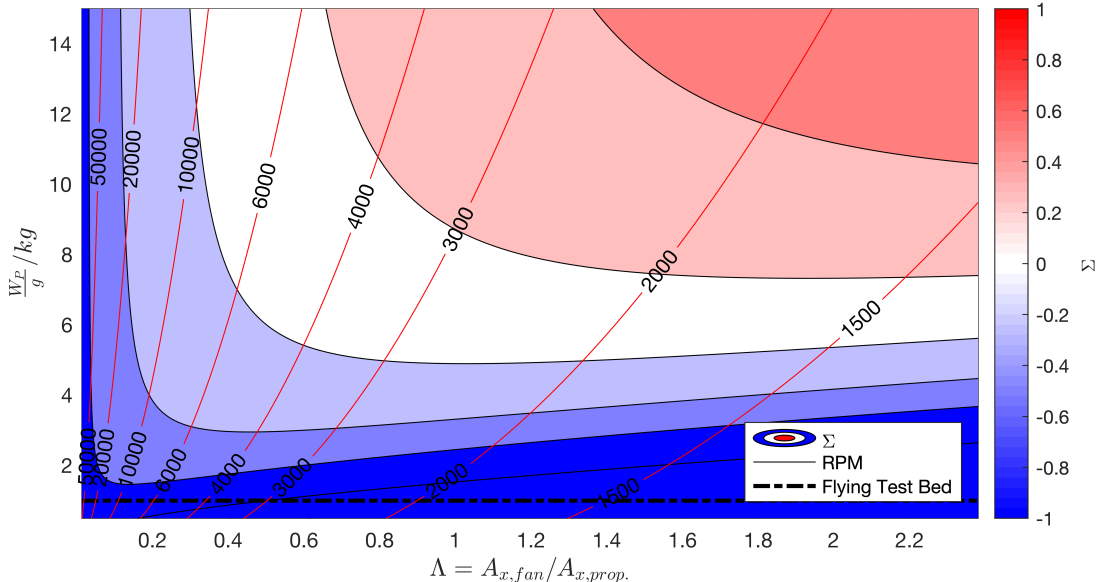


Figure 6.6: Area ratio (Λ) vs. payload (W_P/g) design space showing the superiority parameter given a CFRP construction and experimentally obtained figure of merit. White and red regions are positive, blue regions are negative. The flying test bed design payload is marked with a dashed line showing $\Sigma < 0$ for all Λ .

Figure 6.6 shows regions where this ducted fan satisfies the superiority condition. For a given payload it shows there to be an area ratio that maximises the superiority parameter, Σ , as contours of Σ have a minima. From the range considered it is unclear whether this minima extends to higher payloads. Figure 6.6 shows that provided a minimum area ratio and payload are achieved, the superiority condition is satisfied by the ducted fan.

6.2 Hover Tests

Hover tests were conducted using the VTOL optimised propeller to verify the method. Preliminary results are presented here and compared to those obtained in stationary tests.

6.2.1 Propeller Performance

The figure of merit recorded was $0.29 \pm 0.05 / \eta_{sys.} \approx 0.65 \pm 0.1$. This suggests that in-flight performance is comparable to stationary test performance.

6.2.2 Hover Test Limitations

The error observed in the flight data was large due to variations in thrust resulting from the control system attempting to maintain position. This resulted in frequent spikes in the power. Combining this error with the low sampling rate for power readings made it difficult to determine the exact figure of merit. As the propellers were unshrouded care was taken to avoid contact with the test cage walls which likely resulted in more manual position corrections than necessary. This will improve when testing ducted fans as the casing will provide shielding against contact. As a result of the test environment being small and in close proximity to solid walls, there was significant wall effect further adding to the difficulty to maintain horizontal position. A larger test environment or testing outside on a calm day could be suitable alternatives. More emphasis should be placed on tuning the control system once the ducted fans have been mounted to ensure smooth motion and reduce the magnitude of power spikes.

7 Future Work

This report has acknowledged the open design space for eVTOL vehicles and established the validity of pursuing alternative methods of propulsion to the propeller. Further work is needed to better understand the design space, consider other propulsor configurations, and explore the response of a ducted propulsor in a dynamic environment. These ideas are discussed in this section.

7.1 Propulsor Design

7.1.1 Contra-rotating Ducted Fan (CRDF)

The superiority condition adds a design constraint that enables comparative performance to be determined. Consider the superiority condition, as defined in Eqn. 1.14

$$\Sigma = \left[\frac{(M_{F,s}A_x)_{fan}}{(M_{F,s}A_x)_{prop.}} \right]^{\frac{1}{3}} - \frac{W + \Delta W}{W} \quad (7.1)$$

Assuming fixed figure of merit and comparable $A_{x,fan}$ and $A_{x,prop.}$ this suggests the superiority parameter can be increased in two ways. Firstly the payload could be increased – Fig. 6.6 demonstrates this by evaluating the design at higher payloads. Secondly, thrust density of the propulsor could be increased to reduce the number of propulsors required for hover, thus reducing ΔW . CRDFs replace the stator in a normal ducted fan (NDF) with another rotor spinning in the opposite direction. This means the work done on the flow can double. This increase in work can be ‘cashed-in’ in a number of ways. Assuming each rotor has a flow coefficient and stage loading ϕ_1, ϕ_2 and ψ_1, ψ_2 respectively, considering velocity triangles with rotor 1 relative angles β and rotor 2 relative angles γ , and that axial velocity is constant along the duct

$$\frac{\psi_1 U_1}{\tan \beta_2 - \tan \beta_1} = \frac{\psi_2 U_2}{\tan \gamma_2 - \tan \gamma_3} \quad (7.2)$$

It can further be shown that

$$\tan \alpha_1 + (\tan \beta_2 - \tan \beta_1) = (\tan \gamma_2 - \tan \gamma_3) + \tan \alpha_3 \quad (7.3)$$

Hence assuming axial flow at inlet ($\alpha_1 = 0$) and exit ($\alpha_3 = 0$), using Eqn. 7.3 Eqn. 7.2 becomes simply

$$\psi_1 U_1 = \psi_2 U_2 \quad (7.4)$$

Therefore assuming both rotors are loaded equally during steady operation this suggests they must also have equal rotor speeds. This result is also shown by Waldren *et al.* (2019)^[23]. Waldren also shows that the overall performance of a CRDF stage can be described by considering the pair of rotors in the reference frame of the downstream rotor, such that the machine looks like a NDF with rotor speed $|U_1| + |U_2|$ in a frame of reference rotating at U_2 . As a result the relative frame CRDF non-dimensionals, ϕ' and ψ' , can be related to the absolute frame non-dimensionals, $\phi_{1,2} = \phi$ and $\psi_{1,2} = \psi$ by

$$\psi' = \frac{\phi'^2}{4\sigma^2} \implies \frac{\psi'}{\phi'^2} = 2 \cdot \frac{\psi}{\phi^2} \quad (7.5)$$

As efficiency is governed by the relative frame non-dimensional, this implies that using a CRDF would enable more of the design space to become accessible resulting in higher absolute frame flow coefficients without compromising efficiency. For example keeping $\psi' = \psi$

implies a higher absolute frame flow coefficient can be achieved whilst keeping the relative frame flow coefficient the same as the NDF design. From Eqn. 3.7 and keeping $\psi' = \psi$ gives a absolute frame flow coefficient $\phi = \sqrt{2}\phi'$ resulting in thrust increasing by a factor of 2 meaning half as many propulsors are required and so ΔW decreases. As the relative ducted fan performance is governed only by the figure of merit (a function of exit duct area ratio alone) and flow area (unchanged no matter how many fans are in the passage) the RHS of the inequality will remain unchanged¹. For example a design with area ratio $\Lambda = 1$ and payload $W_P/g = 5\text{kg}$ has $\Sigma_{NDF} = -0.03$ but with a CRDF this becomes $\Sigma_{CRDF} = +0.29$.

7.1.2 Computational Fluid Dynamics (CFD)

Empirical results such as Carter's rule and Lieblein's diffusion factor are obtained from experiments on compressor cascades, assumed to approximate an infinite radius compressor with a finite span. This assumes secondary flow effects are minimal. However for a low HTR design at a finite and small radius, the validity of these correlations is unknown. Loss mechanisms and flow behaviour assumptions could be validated using CFD. McEveley (2020)^[24] explores the use of CFD in ducted fans and demonstrates corroboration with experiment.

7.2 Stationary Propulsor Experiments

The design discussed for fan D in Section 3 must now be tested. It should be manufactured using the higher quality 3D printing settings used for fan C as this showed a significant improvement in diffuser performance and overall figure of merit. A fan characteristic can be obtained by running the fan with varying back pressure to change the operating point. Ideally an exit traverse would also be undertaken to determine stagnation pressures across the annulus and further analyse potential sources of loss. Alternative manufacturing techniques should be considered to satisfy the superiority condition using lighter propulsors. Finally a comparable CRDF design should be tested to verify increased thrust and constant figure of merit for a lower propulsor weight

7.3 Flying Test Bed Experiments

Two developments are considered here to extend the capabilities of the flying test bed. Firstly the addition of various sensors to the flying test bed for static hover tests is discussed. Secondly using the flying test bed to analyse the stability of ducted fans whilst manoeuvring is considered.

¹Evidence suggests small increases in efficiency may be achieved by using a CRDF^[23] and so the actual figure of merit may increase.

7.3.1 Static Hover Test Adaptations

The hover test setup provides multiple interfaces for further data collection through the RPi3. RPM, noise output, and pressures could be added to the flying test bed hover test. Potential setups for these are discussed.

RPM A single RPM sensor could be used during hover tests. To ensure the RPi3 sample rate on the IR photo-transistor output is high enough to register both reflective strips every revolution, only one sensor can be used. For static hover testing this is sufficient as each motor should have approximately equal speeds.

Noise Acoustic noise generated by the flying test bed can be measured by an external microphone kept at a fixed horizontal distance, 1m for example. This allows the noise output by the ducted fan and the propellers to be compared.

Optional Pressure Transducers The ADCPi ADC breakout on the RPi3 allows pressure transducers to be connected directly to the flying test bed. Two breakout boards can be stacked to give a total of $6 + 8 = 14$ inputs pressure transducer readings (2 inputs from the first ADC are used by the horizontal proximity ultrasounds and each ADC has 8 input channels).

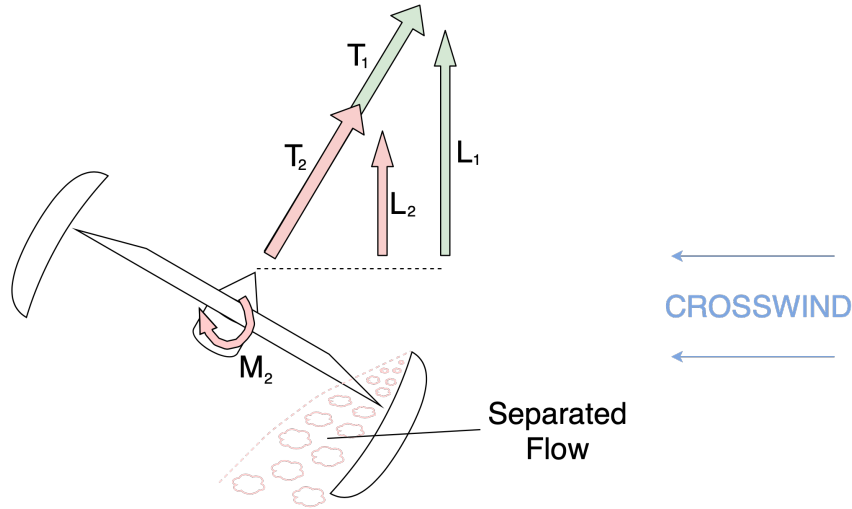


Figure 7.1: Effect of separation of leading lip during horizontal manoeuvre

7.3.2 Manoeuvre Tests

One drawback of the ducted design is the presence of the intake and casing upstream of the rotor. In a crosswind, or during horizontal translation of the propulsor, the flow moves

across the intake and is at risk of separating off the leading edge of the intake. This results in turbulent flow passing into the windward side of the rotor resulting in a destabilising moment on the propulsor. This moment could be measured in a static wind-tunnel environment[5] but the impact on in-flight manoeuvrability is also important. Consider a horizontal manoeuvre in which the flying test bed attempts to achieve a constant horizontal velocity whilst maintaining altitude. The resulting crosswind may begin to separate off the leading lip of the intake, resulting in a decrease in propulsor thrust at the current motor speed. As the propulsor must be angled to provide both forward thrust and lift, a drop in thrust results in a decrease in lift as well as a destabilising moment as in Fig. 7.1. Therefore the control system would demand a higher motor RPM to ensure sufficient lift. One proposed measure of manoeuvre stability is the power requirement to maintain steady horizontal translation at a fixed altitude normalised by the power required for static hover.

8 Conclusions

The following conclusions can be drawn with reference to the research questions posed in Section 1.3

1. A ducted fan was developed with a design figure of merit of 1.51 and achieved $M_{F,s} = 1.36$ in experiment. Aerodynamic efficiency was therefore found to be $\eta_a = 90\%$. Separation, skin friction and shroud clearance flow losses are hypothesised to be the primary sources of loss. Skin friction and shroud clearance flows can be improved using alternative manufacturing methods.
2. The ducted fan did not satisfy the superiority condition when applied to the flying test bed and the superiority parameter is predicted within 2% of the recorded value. Suitable ranges of operation in which the superiority condition is satisfied are identified using the mass model (including for fan-propeller area ratios less than 1) by increasing payload and using CRDFs to reduce the number of propulsors required to achieve static hover.
3. In-flight hover figure of merit was recorded as $M_{F,s} = 0.65$ which agrees with stationary testing in which the figure of merit was evaluated as $M_{F,s} = 0.67$ from manufacturer's calibration data. In-flight data experienced significant noise compared to stationary testing due to the control system attempting to maintain position.

References

- [1] A. T. Institute. (2019). Accelerating ambition technology strategy 2019, [Online]. Available: <https://www.ati.org.uk/media/siybi1mm/ati-tech-strategy.pdf> (visited on 05/20/2020).
- [2] L. Schroth. (2019). The drone market 2019-2024: 5 things you need to know, [Online]. Available: <https://www.droneii.com/the-drone-market-2019-2024-5-things-you-need-to-know> (visited on 01/03/2020).
- [3] R. Thomson. (Jan. 2020). Electrically propelled aircraft developments exceed 200 for the first time, [Online]. Available: <https://www.rolandberger.com/en/Point-of-View/Electric-propulsion-is-finally-on-the-map.html> (visited on 05/20/2020).
- [4] T. Zhang and G. N. Barakos, “Review on ducted fans for compound rotorcraft”, *The Aeronautical Journal*, pp. 1–34, 2019.
- [5] J. L. Pereira, “Hover and wind-tunnel testing of shrouded rotors for improved micro air vehicle design”, MARYLAND UNIV COLLEGE PARK DEPT OF AEROSPACE ENGINEERING, Tech. Rep., 2008.
- [6] E. S. D. Unit, “Performance of circular annular diffusers in incompressible flow”, Engineering Sciences Data Unit, Tech. Rep., 1975.
- [7] A. Maffioli, C. Hall, and S. Melvin, “Aerodynamics of low reynolds number axial compressor sections”, in *53rd AIAA Aerospace Sciences Meeting*, 2015, p. 1934.
- [8] R. Corralejo and P. Harley, “Smith diagram for low reynolds number axial fan rotors”, in *12 th European Conference on Turbomachinery Fluid dynamics & Thermodynamics*, EUROPEAN TURBOMACHINERY SOCIETY, 2017.
- [9] S. L. Dixon and C. Hall, *Fluid mechanics and thermodynamics of turbomachinery*. Butterworth-Heinemann, 2013.
- [10] S. Lieblein, F. C. Schwenk, and R. L. Broderick, “Diffusion factor for estimating losses and limiting blade loadings in axial-flow-compressor blade elements”, NATIONAL ADVISORY COMMITTEE FOR AERONAUTICS CLEVELAND OH LEWIS FLIGHT . . . , Tech. Rep., 1953.
- [11] N. A. ad Tom Hynes, *Cued engineering tripos 4a3 turbomachinery i lecture notes, applications and characteristics of turbomachinery*, Oct. 2019.
- [12] A. R. Howell, “Fluid dynamics of axial compressors”, *Proceedings of the Institution of Mechanical Engineers*, vol. 153, no. 1, pp. 441–452, 1945.
- [13] A. Howell, “Design of axial compressors”, *Proceedings of the Institution of Mechanical Engineers*, vol. 153, no. 1, pp. 452–462, 1945.
- [14] A. D. Carter, *The low speed performance of related aerofoils in cascades*. HM Stationery Office, 1950, vol. 29.

- [15] J. V. Taylor and R. J. Miller, “Competing Three-Dimensional Mechanisms in Compressor Flows”, *Journal of Turbomachinery*, vol. 139, no. 2, Oct. 2016, 021009, ISSN: 0889-504X. DOI: 10.1115/1.4034685. eprint: https://asmedigitalcollection.asme.org/turbomachinery/article-pdf/139/2/021009/6305774/turbo_139_02_021009.pdf. [Online]. Available: <https://doi.org/10.1115/1.4034685>.
- [16] J. Barry, “4th year project report: Propulsion systems for vtol electric vehicles”, Cambridge University Engineering Department, Tech. Rep., Jun. 2019.
- [17] I. Anderson, “Mechanical properties of specimens 3d printed with virgin and recycled polylactic acid”, *3D Printing and Additive Manufacturing*, vol. 4, no. 2, pp. 110–115, 2017.
- [18] A. P. Composites. (Dec. 2014). Performance data for 10x4.7sf, [Online]. Available: https://www.apcprop.com/files/PER3_10x47SF.dat (visited on 05/23/2020).
- [19] H. H. Hubbard, “Sound measurements for five shrouded propellers at static conditions”, 1950.
- [20] J. Qing, Y. Hu, Y. Wang, Z. Liu, X. Fu, and W. Liu, “Kriging assisted integrated rotor-duct optimization for ducted fan in hover”, in *AIAA Scitech 2019 Forum*, 2019, p. 0007.
- [21] J. D. Denton, “The 1993 igt scholar lecture: Loss mechanisms in turbomachines”, 1993.
- [22] OnShape. (2020). Onshape materials library, [Online]. Available: cad.onshape.com (visited on 05/23/2020).
- [23] J. Waldren, C. Clark, S. Grimshaw, and G. Pullan, “Non-dimensional parameters for comparing conventional and counter-rotating turbomachines”, in *Turbo Expo: Power for Land, Sea, and Air*, American Society of Mechanical Engineers, vol. 58561, 2019, V02BT40A026.
- [24] M. McEveley, “4th year project report: Propulsion systems for vtol electric vehicles”, Cambridge University Engineering Department, Tech. Rep., Jun. 2020.

Appendix A: COVID-19

The Coronavirus pandemic resulted in the closure of all University buildings and laboratories on the 22nd of March 2020, as well as an extended period of self-isolation due to illness. This reduced the testing window by 10 weeks.

Tests to Complete

Testing of fan D and complete pressure measurements of fan C were not possible and so fan A, B and C (excluding flow coefficient and stage loading measurements) prototypes were instead used to explore ducted fan performance. These versions were intended to verify and

fine tune the manufacturing process as well as explore design variables. Only hover tests with the APC propeller were carried out.

Adaptations to Final Report

The report focuses on the design process and presents what data is available to back up the design philosophy. Differences between the design section and the final design of the fans came as a result of access to the Whittle laboratory ending. Significant work was done to render the flying test bed and both stationary and hover test setups and environments in the absence of an opportunity to photograph them.

Appendix B: Retrospective Risk Assessment Analysis

The risk assessment produced at the beginning of the project was followed and the project proceeded without incident. In addition to the mitigations discussed in the risk assessment the flying test bed controls were mounted to the outside of the test environment to ensure the anyone controlling the flying test bed had full and unrestricted view of the vehicle in case of emergency.